EXPERIMENTAL AND NUMERICAL VALIDATION OF A FORWARD FACING CAVITY AS A PASSIVE THERMAL PROTECTION SYSTEM OF A HYPERSONIC BODY

by

Tyler Watkins

A thesis submitted to the faculty of
The University of North Carolina at Charlotte
in partial fulfillment of the requirements
for the degree of Master of Science in
Mechanical Engineering

Charlotte

2022

Approved by:

_____

Dr. Keanini R.

_____

Dr. Dahlberg J.

_____

Dr. Cherukuri H.

ABSTRACT

TYLER WATKINS. Experimental and Numerical Validation of a forward facing cavity as a passive thermal protection system of a hypersonic body. (Under the direction of DR. KEANINI R.)

Interest in hypersonic flight has grown rapidly in recent decades, especially within the space and defense industries. As research and development in this area has matured, associated heat transfer phenomena, as well as the aerothermodynamics of hypersonic flight have assumed increasing importance. One continuing challenge centers on ablation at leading edges of hypersonic vehicles. This process drastically changes flight dynamics, and complicates flight performance prediction and vehicle design. In this thesis, both numerical and experimental investigations have been undertaken in order to study the effectiveness of a forward facing cavity on reducing heat transfer at the leading edge of a missile-shaped body. This effort aims to validate the forward facing cavity as a means of reducing heat loads. An additional focus centers on investigating the impact of gas equation of state on predicted fluid dynamics, as well as flow-to-vehicle heat transfer, where hypersonic flows are simulated for bodies having both solid noses and on-nose cavities. It is shown that the introduction of a forward facing cavity reduces overall heat loading. In addition, numerically predicted heat loads are strongly dependent on the gas equation of state used. Physical interpretations of the numerical results provide insight into both gas model choice and the physics of the non-equilibrium flow that exists between a forward bow shock and the missile body.

ACKNOWLEDGEMENTS

I would like to thank all of the Professors within the William States Lee College of Engineering for providing me with a sound education.. Specifically, I would like to thank my Thesis Committee and Advisors: Dr. Russell Keanini, Dr. Jerry Dalhberg, and Dr. Harish Cherukuri. I would also like to thank Dr. Peter Tkacik.

I owe a huge thank you to Dr. Russell Keanini for his time, supporting me in my research and his continued inspiration in a field I am passionate about. I would like to especially thank Dr. Jerry Dahlberg for his time invested in my education, leaderhsip, and mentorship throughout my undergraduate and graduate studies.

TABLE OF CONTENTS

LIST OF TABLES

LIST OF FIGURES

LIST OF SYMBOLS

ρ, Density

τ_{wall}, Wall Shear Stress

C_f, Coefficient of Friction

C_p, Specific Heat

h, Local Convective Heat Transfer Coefficient

M, Mach Number

Nu_x, Nusselt Number

Re_x, Local Reynolds Number

U_∞, Free Stream Velocity

U_{fric}, Friction Velocity

Δs, First Prism Layer Height

δv, Characteristic Boundary Layer Height

CHAPTER 1: INTRODUCTION

1.1 Introduction to Hypersonic Heating

Various factors have led to increased interest in hypersonic flight in recent years. This interest traces back to the beginning of the Cold War and, in recent years, has intensified as nation states seek to build hypersonic transport and weaponry. Hypersonic flight is often described as flight at free stream Mach numbers exceeding five. However, from a physical standpoint, hypersonic flight refers to conditions in near-body boundary layers where a variety of complex, Mach-number dependent processes can emerge, including non-equilibrium flow of gas constituents, ionization and recombination of gas species, emmission and absorption of radiation both within the gas and at the aerodynamic surface, difficult-to-predict laminar-to-turbulent boundary layer flow transition, conversion of high gas enthalpy and kinetic energy into high intensity surface heating, thermal ablation of aerodynamic surfaces, generation of high frequency screech modes, excitation of high frequency in-solid flutter, and various shock-boundary layer interactions.

Predicting and mitigating against intense surface heating and surface stress, particularly at the leading edges of aerodynamic bodies, remains a central challenge in hypersonic aerodynamics. High heat loads and stresses can ablate the leading edge, destabilizing the high speed flow, threatening the integrity of the aerodynamic body, and placing the body well outside its design envelope.

These phenomena are visually represented in fig 1.1. As shown, large heat loads exist along all leading edges, being highest at the nose and decaying, due to boundary layer thickening and reduction of viscous heating, with distance from the nose.

Figure 1.1: Hypersonic Glide Vehicle, Leading Edges Experiencing High Friction and Heat Loading

The aerothermodynamic phenomena that arise during hypersonic flight makes for very difficult mechanical design. This study focuses on the problem of leading edge heating. Here, a potential approach for mitigating against leading edge heating, introduction of a forward facing cavity, placed at the nose of a missile-shaped test body, is investigated in preliminary fashion. Experimental schlieren images of a cavity-free test body, placed in a steady, mach 5 wind tunnel flow, are first obtained. A three-dimensional hypersonic flow model, employing an adaptive meshing algorithm, is first developed and validated against schlieren image data. Three hypersonic flow models, each characterized by a distinct equation of state for the flowing gas, are then used to predict heat transfer from a mach 4.5 flow to both a cavity-free and cavitied test body. Physical and design implications derived from the numerical experiments are then presented.

1.2 Governing Equations

Computational fluid dynamics (CFD) is used to model the steady, high speed flow about the test bodies. For this thesis, the software package Star CCM+ is used. Due to the presence of extreme velocity and temperature gradients, produced by a leading bow shock, as well as body-adjacent viscous and thermal boundary layers, mesh generation assumes central importance in obtaining reliable flow and heat transfer results. Here, as detailed below, automated mesh refinement is used.

Star CCM+ provides the user with two different solver options, coupled and segregated. Due to strong coupling and interchange extant between momentum and energy in high speed flows, the coupled solver is used here. Thus, mass, momentum and energy equations are solved simultaneously.

CFD Governing Equations:

A central assumption underlying the Navier-Stokes equations states that at all points and times within a given flow, the flow exists in a state of local thermodynamic equilibrium (LTE). LTE, in turn, requires that the so-called local flow time scale, $\tau_{flow} = L_{ptcl}/U$, is much longer than the molecular equilibriation time, τ_{equil}, where L_{ptcl} is the length of, say, a cubical, fixed mass fluid particle containing N molecules, and U is the magnitude of the local (vector) bulk fluid velocity (=the instantaneous vector sum of the molecular velocities within the fluid particle, divided by N). Under all but the most extreme conditions, and for fluid particle dimensions on the order of 10^{-6} to 10^{-7} m, in a Newtonian fluid, e.g., air and water, $\tau_{flow}/\tau_{equil} >> 1$. In other words, over the (short) time required for a fluid particle to traverse its own length, τ_{flow}, the N molecules constituting the particle typically achieve thermodynamic equilibrium.

Unfortunately, from a modeling perspective, hypersonic flow regions behind shocks and within boundary layers typically do not achieve LTE. Local nonequilibrium can arise due to a variety of processes, including the following: a) molecular vibrational

modes in oxygen and nitrogen, excited by passage through high (flow direction) shear within shocks, relax on time scales that are long relative to τ_{flow} ; b) molecules that are ionized both by flow through shocks and flow within high shear, high temperature viscous and thermal boundary layers can likewise recombine on time scales long relative to τ_{flow}, and c) molecular emission and absorption of radiation, and associated collisional thermal equilibriation, can again be slow relative to τ_{flow}.

Due to the predictive power of the Navier-Stokes equations, at least for flows of Newtonian fluids satisfying LTE, the NS equations have been adapted to nonequilibrim flows, using approaches that essentially amalgamate the NS equations with schemes designed to accommodate nonequilibrium processes. For reviews of some of these approaches, see, for example, [6].

In this thesis, the Navier Stokes equations are used to solve the mass, momentum, and energy conservation equations. The dominant nonequilibrium processes that are likely extant in our experimental system include slow relaxation of vibrational modes in molecular oxygen and nitrogen, and to a lesser degree, dissociation and recombination of these molecules, as well as other constituents in atmospheric air. As detailed below, Star CCM accommodates these processes via three phenomenalogical equations of state, incorporated with the NS framework.

Thus, starting from a stagnation (zero velocity) initial condition, the governing equations are simultaneously solved using an implicit time scheme (see below), with computations stopped when . numerical stopping criteria is reached. The solver used by Star CCM is a finite volume solver, thus each cell in the mesh continua makes up a control volume that contains a solution. Therefore the equations are solved in integral form. In Star CCM+ The equations are solved as a vector of equations 1.1 giving the governing equations written in integral form a given surface area and volume. The momentum equations resolve the velocity gradients, continuity the pressure and the equation of state calculates the density. [7]

$$\frac{\partial}{\partial t}\int_V \mathbf{W}dV + \oint [\mathbf{F} - \mathbf{G}] \cdot d\mathbf{a} = \int_V \mathbf{H}dV \tag{1.1}$$

For each of the surface integrals in eqn 1.1, Vectors W, F, G and H are defined as shown below and 1.1 further defines the value for each vector definition. It is also important to note the value of total energy per unit mass is a function of total enthalpy, which is a function of specific heat and ultimately temperature [7].

$$\mathrm{W}=\begin{bmatrix} \rho \\ \rho\mathbf{v} \\ \rho E \end{bmatrix}, \quad \mathbf{F} = \begin{bmatrix} \rho\mathbf{v} \\ \rho\mathbf{v}\mathbf{v} + p\mathbf{I} \\ \rho\mathbf{v}H + p\mathbf{v} \end{bmatrix},$$
$$\mathrm{G}=\begin{bmatrix} 0 \\ \mathbf{T} \\ \mathbf{T}\cdot\mathbf{v} + \dot{q}'' \end{bmatrix}, \quad \mathbf{H} = \begin{bmatrix} S_u \\ \mathbf{f}_r + \mathbf{f}_g + \mathbf{f}_p + \mathbf{f}_u + \mathbf{f}_\omega + \mathbf{f}_L \\ S_u \end{bmatrix} \tag{1.2}$$

Notation	Value
ρ	Fluid Density
V	Velocity of the fluid
E	Total energy per unit mass
p	Pressure
T	Viscous stress tensor
$\dot{q}''$	Heat Flux Vector
H	Vector of body forces

Table 1.1: Defined Values For Solution of Matrices.

Turbulence Modeling:

The K-Omega Menter SST turbulence model is chosen for all simulations. This model makes use of the K-Omega and K-Epsilon turbulence models. The purpose of this model is to use the K-omega model in the boundary layer, where it is superior at resolving the small scale turbulence. A blending function is then used to blend the K-Omega to the K-Epsilon model in the free stream; there, the less sensitive latter model is used to solve the large eddies in the free stream.

In order to ensure accurate prediction of the laminar to turbulent boundary layer transition location, which is crucial to capturing localized surface heating at the transition point, it is important to properly define a thin prism layer adjacent to the solid surface . Moreover, proper accounting of heat transfer at the boundary surface, as well as accurate modeling of viscous effects within the viscous boundary layer, rests on proper selection of the prism layer thickness, Δs. In order to choose Δs, a non-dimensional y+ value is introduced, where y+ can be interpreted as a near-surface Reynolds number, $y^+ = \rho U_{fric} \Delta s / \mu \, (Re_{fric})$. Here, the near-surface velocity scale, U_{fric}, termed the friction velocity, determined by the local wall shear stress, determines the local Reynolds number (and the local y^+). Dynamically, since Re_{fric} is

roughly proportional to the ratio of the near-surface flow inertia (of a near-surface fluid particle) to the near-surface viscous force on the particle, the near-surface thickness, Δs, is chosen so that y^+ is on the order of 1. The near-surface layer over which y^+ 1, is called the viscous sub layer; it is traditionally viewed as the inner-most region of any turbulent boundary layer.

Thus, the first layer height, Δs, is determined using

$$\Delta s = \frac{y^+ \mu}{U_{fric} \rho} \tag{1.3}$$

where, as discussed below, y+ is a pre-determined or desired value for the particular turbulence model being used.

In detail, the calculation of Δs proceeds as follows. First, a local Reynolds number, Re_x, is calculated using equation 1.4. In contrast to the global Reynolds number, $Re = \rho U_\infty L/\mu$, Re_x uses the distance, x, from the test piece nose, as the reference length:

$$Re_x = \frac{\rho U_\infty x}{\mu} \tag{1.4}$$

Once Re_x is calculated, the coefficient of friction, C_f, is then determined using the correlation [8]:

$$C_f = \frac{0.026}{Re_x^{1/7}} \tag{1.5}$$

The coefficient of friction is then used to calculate wall shear stress:

$$\tau_{wall} = \frac{C_f \rho U_\infty^2}{2} \tag{1.6}$$

which, finally, allows estimation of the friction velocity (often referred to as u star in the turbulence literature):

$$U_{fric} = \sqrt{\frac{\tau_{wall}}{\rho}} \tag{1.7}$$

Given, U_{fric} and a chosen y+, equation 1.1 then gives an appropriate first prism layer thickness, Δs.

The law of the wall, a reasonable model of mean velocity profiles outside the viscous sublayer, but still well within a given turbulent boundary layer, is used to predict the near-surface mean velocity.The law of the wall, is used to predict the mean velocity profile near the wall boundary. This is done by assuming that the turbulence near the wall is behaving independently from the free stream flow regime. This near wall region is described in figure 1.2. When constructing the structured mesh the prism layer mesher is used near the wall to capture the boundary layer. The height of the first prism layer should fall in the viscous sublayer region of the inner layer to capture the viscous effects at the wall. This is especially true for a turbulent boundary layer where the first prism layer height (Δs) should be in the viscous sublayer where the dimensionless velocity u+, often referred to as the friction velocity, is equal to the dimensionless distance y+ (figure 1.2). It is imperative the y+ be below 1 if heat transfer effects are being considered in the simulation; ensuring the viscous effects closest the wall are accounted for and accurately modelled [1].

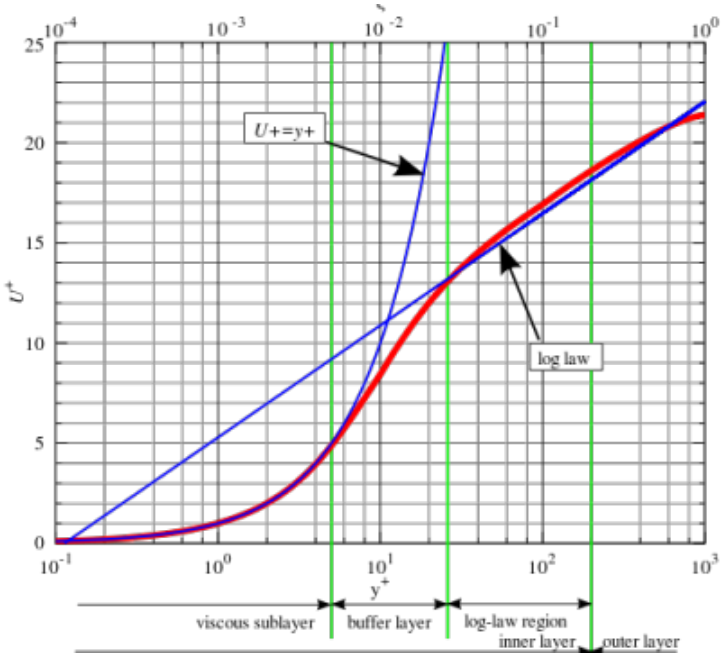

Figure 1.2: Law of the Wall [1]

Heat Transfer

As noted, the aerothermodynamics of hypersonic flight are dominated by large heat fluxes at leading edges. Similar heat loads can be found on other surfaces normal or near-normal to the direction of an incoming flow. Indeed, leading edge heating has proven to be one of the main challenges in high speed flight vehicle design. The intensity of local surface heat transfer is strongly dependent on the nature of the flow boundary layer. Specifically, in laminar boundary layer flow regions where the normal component of free stream velocity is small relative to the tangential (body-parallel) component, e.g., at locations not too close to a leading edge, relatively weak normal-direction convective heat transport takes place. By contrast, in regions where the boundary layer is turbulent, much larger normal-direction transport of heat, produced by boundary layer turbulent eddies, is extant.

In addition, strong local heating can take place at the laminar-to-turbulent boundary layer transition line, in particular, when a separation bubble forms. Here, due to strong normal convective heat transport, produced by the reattaching boundary

layer, a localized spike in surface heat transfer can occur. Importantly, transition typically occurs when the local Reynolds number, Re_x, exceeds 500,000.

Determining local boundary heat transfer between the flowing gas and body surface is carried out using an experimental correlation for the Nusselt number, Nu, defined as:

$$Nu_x = \frac{hx}{k} \tag{1.8}$$

where h is the local convective heat transfer coefficient:

$$h = h\left(x\right) = \frac{\dot{q}}{T_f - T_w} \tag{1.9}$$

x is the body position dowstream of the nose, and k is the temperature-dependent gas thermal conductivity. In addition, T_f and T_w are the local fluid and body surface temperatures, and $\dot{q}$ is the local wall surface heat flux.

Since the local Nusselt number, Nu_x, depends on the local free stream Reynolds number,

$$Re_x = \frac{\rho U_\infty x}{\mu} \tag{1.10}$$

estimation of the local heat transfer coefficient, $h\left(x\right)$, is carried out by first determining Re_x, which when used in the experimental correlation, $Nu_x = f\left(Re_x\right)$, yields $h\left(x\right)$ [9] .

1.3 Equations of State

Equations of state for fluids are typically empirical, but in some cases, theoretical relationships that connect fluid density, temperature and pressure, over a range of fluid sates and conditions. In this study, three equations of state are introduced, each representing differing levels of approximation regarding the complex PVT behavior of high mach number hypersonic flow. One of this study's main objectives centers on examining how predicted body surface heat transfer changes as the gas equation of

state changes. This examination, as discussed later in this thesis, exposes the importance of properly accounting for molecular relaxation processes as high speed flows pass through bow shocks that are a ubiquitous feature of hypersonic aerodynamic flows.

The first and simplest equation of state is the ideal gas law. As detailed later, this model assumes that relaxation of molecular energy modes, excited by passage of gas molecules through shocks, relax on time scales that are short relative to so-called flow time scales, $\tau_{flow} = L_{scale}/U_{scale}$, the latter determined by characteristic (macroscopic) flow length and velocity scales, L_{scale} and U_{scale}. Since the relevant length scale in the present study is the small, millimeter-scale distance from the bow shock to the (shock-inducing) missile nose, and since the flow speed is high, we will find that the implicit assumption of fast relaxation is likely not valid within the crucially important flow region between the bow shock and body.

Ideal Gas Model

The ideal gas law is defined as follows:

$$\rho = \frac{p}{RT} \tag{1.11}$$

where P, T, and ρ, are respectively, pressure, temperature and density. To account for the large temperature excursions seen in high speed flow, the isobatric specific heat is expressed as a polynomial function of temperature:

$$C_pT = C_0 + (C_1 \cdot T) + \left(C_2 \cdot T^2\right) + \ldots + (C_{pn} \cdot T^n)$$

The coefficients and the order of the polynomial used are determined by the user-defined temperature range expected for the given flow problem. For all ideal gas flow simulations in this study, the default coefficients provided by Star CCM+ were used. For regions away from shocks, this model has been shown to be simple, but

robust for modelling hypersonic flows [3]. Sutherland's law is used to compute thermal conductivity and viscosity of the fluid.

Real Gas Model

When using the real gas model in Star CCM+, one option provided to the user is the equilibrium air solver. This model is preferred for high speed flows where high temperature effects cause molecular dissociation, ionization and internal energy excitation. The equilibrium air assumption is that these reactions occur much faster than the times scales of the flow regime. Star CCM+ defines all flow properties for this scenario as a function of temperature and pressure, whose values are predefined in curve fits that account for the thermodynamic and transport properties of the flow regime [10]. These curve fits apply for any flow where the maximum temperature is not above 30,000 K.

Two Species Thermal Non-Equilibrium

Investigation of a thermal non-equilibrium case was carried out by simulating a two species gas model composed of appropriate mole fractions of oxygen and nitrogen. The thermal non-equilibrium model assigns different temperatures to molecular translational and rotational energy modes (both having the same temperature), and vibrational and electronic energy modes. In order close the problem associated with the additional temperature, Star CCM uses an additional energy equation for the conservation of vibrational and electronic energy, which is simplified for non-ionizing flow. Thermal conductivity and viscosity for the mixture is computed using an averaging technique, while individual species thermal conductivities are defined by non equilibrium kinetic theory [7].

1.4 Thesis Structure

Chapter 1: Chapter one gives an introduction to hypersonics and the specific topics of hypersonic heating that is covered in this study. It also covers the governing equations and models that are used throughout the remainder of the thesis.

Chapter 2: Chapter two gives a more specific overview of the forward facing cavity and the motivation to further study this topic, along with previous work done on the subject and important results from those studies.

Chapter 3: Chapter 3 is an overview of the experimental setup. Including and overview of the hypersonic wind tunnel and the schlieren imaging system.

Chapter 4: Chapter 4 covers validation of the numerical models. An in depth breakdown of the computational setup and results validated by experimental results.

Chapter 5: Chapter 5 is the results section. In this chapter experimental and numerical results are examined. Numerical results compare heat flux for the baseline and forward facing cavity case. Along with a comparison of those effects with the different gas models in consideration.

Chapter 6: This chapter summarizes the work and draws together important conclusions from the results of experimental and numerical cases.

CHAPTER 2: MOTIVATION

2.1 Overview of Thermal Protection Systems

In order to overcome the thermal loading on the leading edge of a hypersonic body. Thermal protection systems are often used to control magnitude of heat transferred to the surface. Thermal protection systems are categorized into passive and active systems. Passive systems take advantage of geometric modifications or reactive coatings that do not require a feedback loop to decrease heat flux at the surface of the vehicle. Some common examples of this would be the aerospike design, reactive coatings designed for controlled ablation and other aerodynamic designs that use geometry to control pressure gradients aimed at creating a shear layer in a specific region of the flow regime. Active thermal protection requires a feedback loop and some form of work to operate effectively. Often times these active systems require, plumbing, wiring and other inherent aspects of functionality that are far too complex for conditions during hypersonic flight.

2.2 Previous Work

Overcoming the aerodynamic challenges faced in hypersonic flows by means of passive thermal protection systems dates back several centuries. Some of the earliest work done in the investigation of a forward facing cavity was conducted Saravannan [11] and colleagues. This work continues as more in wind tunnel testing is being conducted to better quantify the dynamic responses of forward facing cavities for a range of free stream conditions. These efforts along with other passive drag and thermal protection systems are given in a robust synopsis by Whang [12]. Some of the early experimental results carried out by Saravannan [2] show the physical

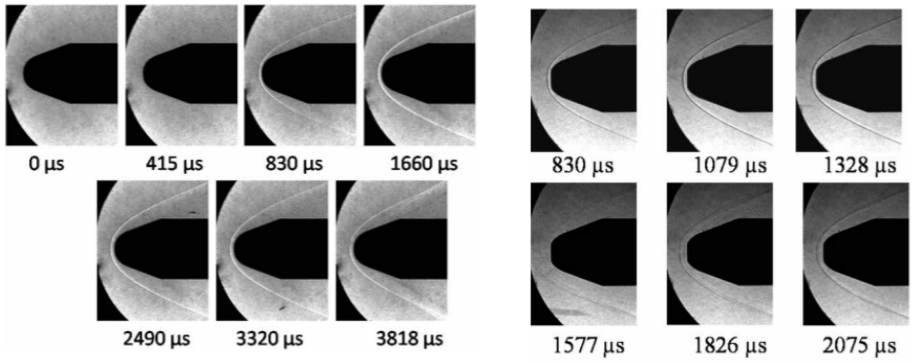

Figure 2.1: Experimental Results Showing the Delta of Shock Detachment Distance Distance From a Baseline to Forward Facing Cavity [2]

phenomena on an increased shock detachment distance for the transient experimental conditions. With the overall goal of the experiments being to investigate the bow shock behavior and resulting changing in surface temperature and heat flux. This was further investigated and confirmed by [13]. Figure 2.2 shows early schlieren imaging captured by Saravannan [2] of a forward facing cavity vs the baseline case.

Saravannan [2] and colleagues also discovered the forward facing cavity weakens the formation of the shock wave leads to decreased wave drag on the vehicle. Numerical studies of the forward facing cavity show the same trends of experimental data and imagery. One of the most notable being Saravannan [11] 2011, quantifying the magnitude of heat flux reduction at the leading edge of the body. Numerical investigations have also been carried out on various cavity geometries such as parabolic cavities as carried out by Yadav [14]. Studies conducted by Yadav and colleagues show a drastic increase in the vorticity in the parabolic cavity vs the cylindrical cavity. Additionally, a range of cylindrical cavity geometries have been studied to better understand how Length to diameter ration effects normal shock width and shock detachment behavior. Figure 2.2 shows a portion of the results from Saravannan, in this particular study there was an in depth analysis of length to diameter ration and its effect on the mach wave structure and resulting drag force.

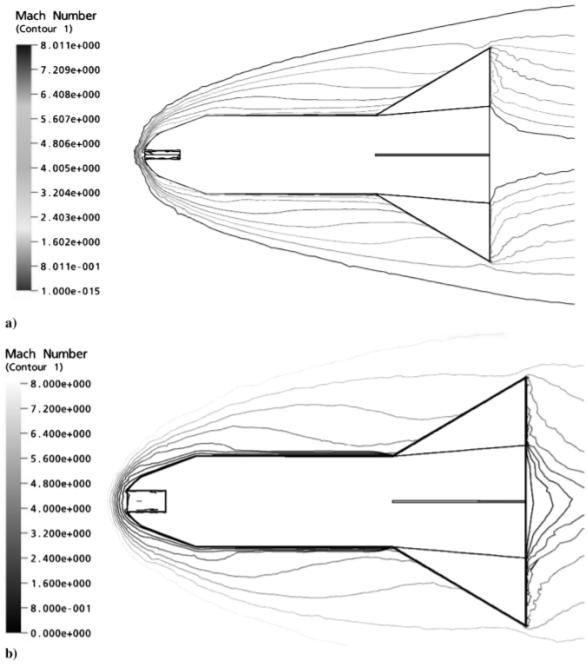

Figure 2.2: Results From Numerical Investigation by Saravannan on the Mach Wave Structure For Two Different Cases of Froward Facing Cavity.

Star CCM+ is widely used for flow regimes smaller Reynolds numbers. However, it has also emerged as a viable commercial software option for simulating high speed flow regimes. One such exploration of viability and capability of Star CCM was carried out by Cross, P.G. and West, M.R [3] as part of a multi-phase summary. They conducted out an in depth research on simulating hypersonic flows with Star CCM+. This work explains in detail, preferred solvers settings, mesh refinement techniques and a very detailed analysis of the different gas models available in Star CCM+. All of these settings were carried out of various geometry to explore different phenomena dominant in hypersonic flows. Figure 3.3 shows a comparison by Cross and West of multiple species gas models and their effect on the re-circulation region in a shock wave boundary layer interaction on a double cone geometry.

Work done by Cross and West created a strong database and strategy for modelling any hypersonic flow in Star CCM+; developing standardized mesh refinement criteria for a range of hypersonic cases. This study also contributes to modelling reacting

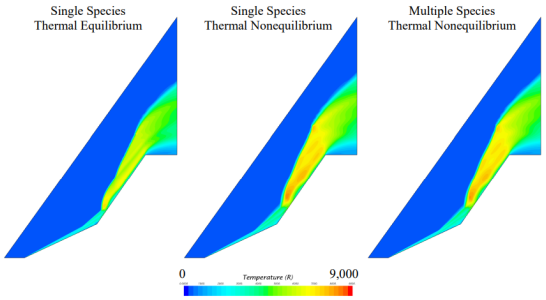

FIGURE 23. Comparison of Temperature Distribution as Predicted by Different Simulations for Double Cone Run 80.

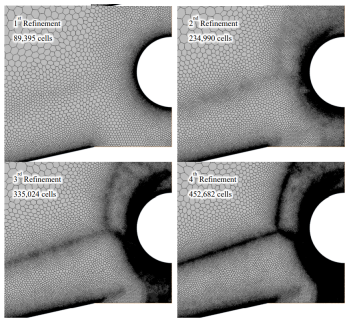

FIGURE 9. Example of Mesh Refinement Using Initial Pressure Gradient Technique.

Figure 2.3: Temperature Gradients Comparison for Double Cone With Different Gas Models Applied and Mesh Refinement at Four Stages of Refinement. [3]

flows using various species gas models and thermal non-equilibrium cases. Solver settings and physics setup to aid in solution convergence of simulations with complex geometries and multiple species gas models Preferred turbulence models and their respective settings for specifics regimes of interest were also explored. Figure 2.3 shows images of the mesh refinement scheme and temperature distribution of various gas models explored in the study. Notice the increase in cells and increase in mesh refinement in the regions of highest pressure gradient.

CHAPTER 3: EXPERIMENTAL SETUP

3.1 Introduction

All experiments were carried out on the Hypersonic Wind Tunnel in the Motorsports Research Lab at UNC Charlotte. The Hypersonic Wind Tunnel is a blowdown tunnel with a 4 hour charge time. Modular nozzle design allows the capability of maintaining an incoming flow of close to Mach 5 for approximately 15 seconds. Operating pressure for the hypersonic tunnel is between 2000-2400 psi. Once fully charged, the software system of the tunnel is used to release the pressure from the tanks via a quick valve. The high pressure flow moves through the plenum, then through the inlet of the nozzle. All nozzle designs are that of a convergent-divergent nozzle, meaning that: a) the flow from the low speed plenum to the throat is subsonic, but accelerating, b) the nozzle throat is sonic, Mach number = 1, and c) flow within the diverging nozzle section is supersonic and, again, accelerating. The dimensions of the supersonic test section downstream of the nozzle are 8" x 12". As detailed in [15], the nozzle contour was designed using a standard method of characteristics approach, wherein the plenum pressure and temperature, as well as the nozzle exit-to-throat area ratio determine the test section Mach number. In the current design, the latter ranges from 3 to 5, depending on the nozzle contour used. As an aside, it is noted that achieving test section Mach numbers in excess of 5 will require preheating of the compressed air. In addition to allowing higher test section Mach numbers, preheating also circumvents formation of condensation shocks, produced when nozzle temperatures drop below the condensation point of molecular oxygen (90 K).

Once high speed air passes through the test section, it exits through a diffuser and silencer to the surrounding atmosphere. Figure 3.1 shows the hypersonic wind tunnel

at UNC Charlotte. Observation of the figure shows the various components of the wind tunnel along with its operating system and Data acquisition system. As detailed in the Masters thesis of Michael White [5], the tunnel was designed and built at UNC Charlotte.

Figure 3.1: UNCC Hypersonic Wind Tunnel [4]

3.2 Schlieren Imaging

As the working gas, in this case air, flows through the test section, a schlieren imaging system is used to capture density gradients within the flow. Here, refraction of white light passing through these gradients allows visualization of the density field. This is due to gases linear relationship between refractive index and density.

The Schlieren imaging system used in the experiments consists of: a) two slightly concave mirrors, each of a 5" diameter, positioned in a so-called Z-configuration; see figure 3.3; b) a collimated white light source generated from a incandescent bulb that passes through a condenser lens. This light then collimated and passed through the test section where the density gradients in the flow regime change the refractive index of the collimated light. These gradients are then captured by a high speed camera at a knife edge where the beam reaches its focal point This light passed

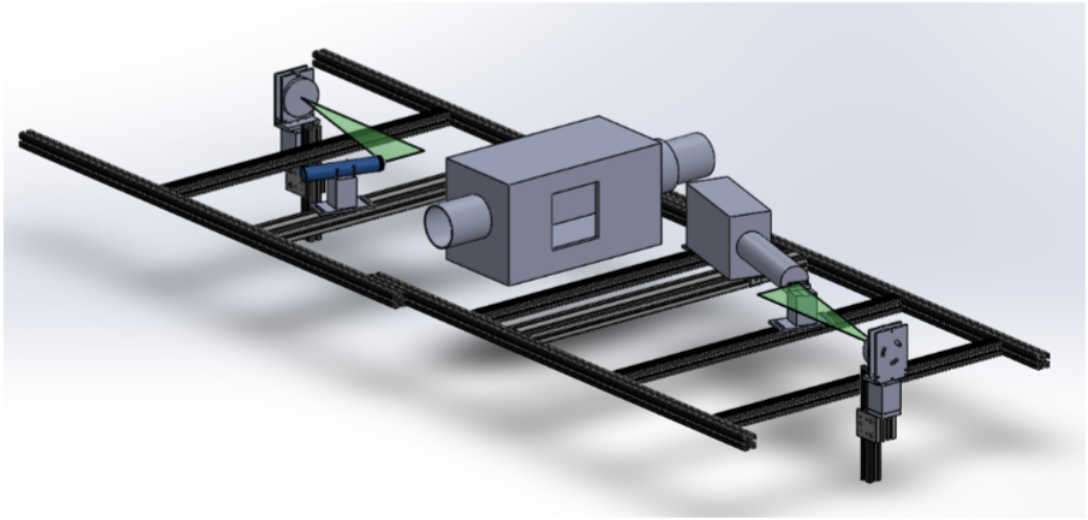

Figure 3.2: Schlieren Imaging Setup. Credit: Michael J.White, University of North Carolina at Charlotte.

3.2.1 Details of Schlieren set-up

Pre-adjustment preparations are necessary for proper operation of the schlieren imaging setup. Firstly, it is important to keep the mirror surfaces clean, avoiding touching the mirrors as they are very delicate optical surfaces. In the event that the mirrors are touched, do not attempt to wipe the mirrors off, as this could damage the mirror surface. During initial alignment, following initial positioning of the first mirror, perform an initial alignment of the second mirror. Install an aligning flashlight in its designated position on the table and remove both lens covers from the mirrors. Check both mirror supports to ensure the mirrors are fastened to the stand and that they do not move during rough initial alignment.

Initial Rough Adjustment of the first mirror: Adjusting the left to right azimuth is performed using a rotary stage that allows fine adjustments of the mirror azimuth. Aligning the azimuth direction is carried out by turning on the light source and then adjusting the first mirror until a reflection is observed from the second mirror. The azimuthal direction for mirror one is adjusted until one observes maximum reflection from mirror two. Extra care must be taken taken during this step, using

fine, cautious adjustments of the mirror azimuth. Occasionally, there are instances where it is necessary to make alignment up and down, as well.

Flashlight focal length adjustment: Using a flashlight as a stand-in for the Schlieren light source, adjust the focal length of the flashlight until the reflection of the flashlight in both mirrors is of equal size. Once complete, the stage can be locked in place to allow for collimating of the first mirror.

Collimating the first mirror: Once the flash light focal length is properly adjusted, fine adjustments to the first mirror are made. Here, the azimuth is re-adjusted to ensure that the light is horizontally centered on the reflector cover. This is repeated for the vertical alignment, ultimately ensuring that the light is centered on the mirror. This is a crucial step and if performed incorrectly, nonuniform resolution of the imaged flow region results.

Alignment of the camera and knife edge: The center line of the camera should be angled exactly along the reflection angle of the second mirror. In turn, the knife edge is placed at the focal point of the second mirror (23 inches in the present set-up), with its edge placed at the vertical center line of the camera and second mirror. Once complete, the camera and knife edge are locked in place.

Once the light source and camera are aligned on the frame, the second mirror is adjusted. First, the focal length of the mirror is found. Then, the mirror azimuth is adjusted until the focal point is horizontally aligned with the knife edge. Finally, mirror vertical adjustment is made and the stage is locked.

Fine alignment of the Schlieren knife edge was the final step in the experimental setup. Here, following alignment on the vertical center lines of the the camera and second mirror, electronic knife edge positioning is performed via motion studio software. The software allows, for example, zoom settings and basic fitting of the image to the screen. Finer adjustments to the knife edge were also made in this step, specifically, optimizing the horizontal distance between the knife edge and second mirror.

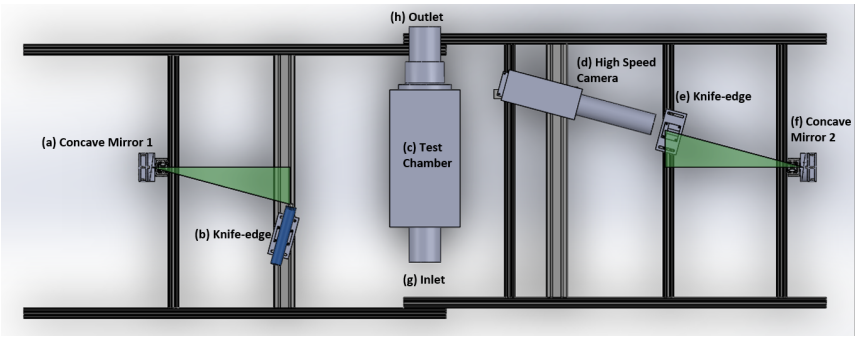

Figure 3.3: Schlieren Imaging Setup. Credit: Michael J.White, University of North Carolina at Charlotte.[5]

Test run: Once the Schlieren imaging system set-up is complete, a very short test run is conducted in order to ensure alignment and functionality of all components of the system. In order to perform a test, lights in the lab are turned off and testing is conducted in the early morning in order to minimize ambient light. Aside: Removal of the knife edge allows shadow-graph imaging. Although shadowgraphs were not gathered in this study, they may be preferred/obtained in future work.

Obtaining the free stream Mach number is carried out via the instrumentation and data acquisition system designed and built for the UNC Charlotte hypersonic wind tunnel [5]. Using the data acquired, the Rayliegh Pitot tube equation is used to calculate the experimental mach number obtained during every Schlieren imaging run. 3.1.

$$\frac{P_t}{P_s} = \left[\frac{(\gamma+1)^2 M^2}{4\gamma M^2 - 2(\gamma-1)}\right]^{\left(\frac{\gamma}{\gamma-1}\right)} \left[\frac{1-\gamma+2\gamma M^2}{\gamma+1}\right] \tag{3.1}$$

Pitot tube static pressure is measured in the test chamber of the tunnel and stagnation pressure in the plenum section of the tunnel. P. Tkacik (personal communication, September 27, 2021).

CHAPTER 4: Validation Case

The validation case is used to validate the simulation domain, solver, physics setup and mesh of the computational setup. This is done using a baseline no cavity case and then results are compared to schlieren imaging results from experiments conducted on the hypersonic wind tunnel. Numerical schlieren imaging is used for visual comparison of the experimental schlieren imaging results. Experimental imaging is also refined using an object detection code that allows for a clearer interpretation of aspects in the flow regime.

4.1 Simulation Domain

Before the physics can be modeled the simulation domain must first be defined. Model geometry was designed in a commercial CAD software, then imported into Star CCM. A series of subtract operations were conducted in Star CCM to create what would become the fluid free stream, along with a symmetry plane that was used to visualize the flow regime. Since the geometry of interest is a symmetric body, a half sphere was created and then mirrored when necessary to visualize the full three dimensional flow regime. The forward facing cavity, and the baseline model both shared the same length L. The spherical domain in which the flow was resolved was constructed such that its boundaries would not interfere with the solution. Both test shapes, each having a length of 30mm, were placed in the forward half of a 150mm spherical domain. This was done in order to minimize the affect of the far field boundary on the downstream solution, to allow full development of the computed downstream flow, and to optimize the computation by moving the model forward of center where uniform free stream conditions exist. The solution domain, modeling

three dimensional flow about the cylindrical, axisymmetric test shapes, is shown in figure 4.1.

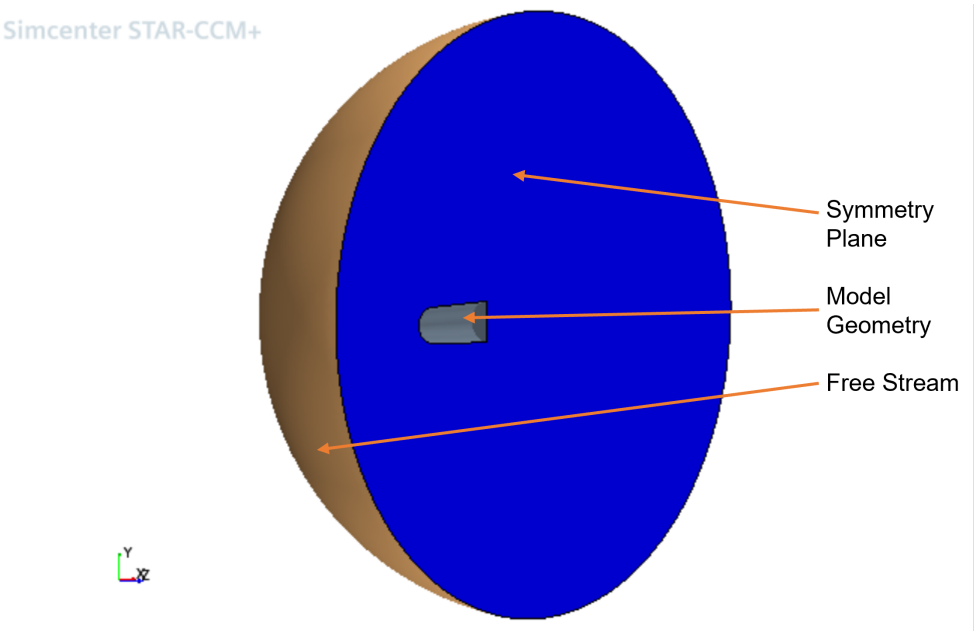

Figure 4.1: Solution Domain

4.2 Boundary Conditions

Boundary conditions were set to mimic an incoming, uniform flow at atmospheric pressure and temperature, having a free stream Mach number of 4.5. The solution domain consists of a half sphere, where flow symmetry is assumed about a plane splitting the sphere in two. The symmetry plane passes through a longitudinal cross section of test body. Flow direction was set such that the incoming flow is perpendicular to the cross sectional area of geometry. Figure 4.1 shows the simulation domain, with the assigned boundary conditions notated for reference.

Hemispherical Far Field Boundary

The hemispherical surface of the half sphere was assigned free stream boundary conditions. Flow direction, free stream speed, pressure and temperature were thus defined on this boundary.

Symmetry Plane

Symmetry conditions were applied to the flat, circular symmetry plane. This condition allows the results of the numerical solution to be reflected about the symmetry plane to obtain a full three dimensional solution.

Model Surface: No-Slip and No-Penetration Conditions

The model surface was assigned no-slip and no-penetration conditions. As discussed below, the combination of no-slip and high free stream speed generates a thin viscous boundary layer and, in turn, significant frictional heat generation, i.e., viscous dissipation, within the boundary layer. This physical effect underlies the chosen thermal boundary condition.

Isothermal Temperature Condition

For the validation case, and all other cases, the wall thermal condition at the surface pf the geometry is set to a fixed temperature of 1000 K. A simple scaling argument can be used to show that this is a reasonable idealization. This argument begins with the Cartesian, steady, incompressible energy equation applied for a thin viscous boundary layer, shown in equation 4.1. A free body diagram, figure 4.2 provides reference to the nomenclature and application of the equations used in the argument.

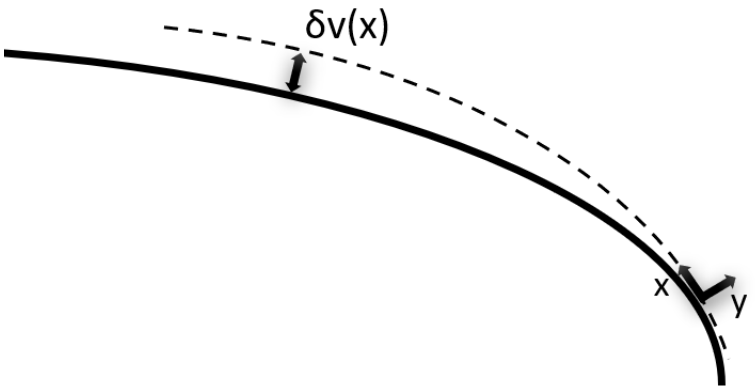

Figure 4.2: Wall Thermal Condition Free Body Diagram

Referencing figure 4.2 in application of the energy equation applied for a thin viscous boundary layer, x is the stream-wise position and y is the local normal direction.

$$UT_x + VT_y = \alpha T_{yy} + \frac{\upsilon}{\rho Cp} (U_y)^2 \tag{4.1}$$

First, equation 4.1 is balanced by the dominant in the equation, from the equation we are seeing that the convective heat transfer must be on the same order of magnitude as the frictional heating term.

$$UT_x \sim \frac{\upsilon}{\rho Cp} (U_y)^2 \tag{4.2}$$

Then, replacing the last term on the right side of equation 4.2 with the appropriate terms for order of magnitude yields equation 4.3

$$U_\infty \frac{\Delta T}{L} \sim \frac{\upsilon}{\rho C_P} \left(\frac{U_\infty^2}{\delta v^2} \right) \tag{4.3}$$

Where the characteristic boundary layer thickness is defined as equation 4.4 and temperature delta acorss the length of the vehicle is defined as equation 4.5.

$$\delta_v = \sqrt{\frac{\nu L}{U_\infty}} \tag{4.4}$$

Solving equation 4.3 for the temperature delta yields equation 4.5. From this equation we are able to solve for the temperature at the surface of the hypersonic body.

$$\Delta T \sim \frac{U_\infty^2}{C_p} \tag{4.5}$$

where:

Cp = $10^3 \frac{J}{Kg*K}$

$U_\infty = (4.5)(340 m/s) = 1530 m/s$

When solved we get delta T equal to 2340K. Thus the imposed constant temperature boundary condition was set to 1000K, shown in equation 4.6, as an approximation roughly corresponding to the average surface temperature across the length of the body from x=0 to x=L.

$$T_{surf} = T(x, y = 0) = 1000\text{C} \tag{4.6}$$

This assumption and boundary condition was applied to the validation case and all investigative cases ran following the validation case.

4.3 Model Geometry

The model geometry used for the validation case was that of the baseline-no cavity case. This geometry is was used in the validation case to ensure a simple geometry in the hypersonic wind tunnel that would yield good schlieren imaging and clear mach wave development and bow shock detachment distance for means of validation to numerical results. The test section of the hypersonic wind tunnel is also sensitive to larger diameter models. Model diameters that are too large create mach reflections within the test section and result in interrupted schlieren imaging. These factors drove the development of the size and shape of the validation model. As shown in figure 4.3, the model geometry can be considered a pseudo blunt body; the leading diameter is 0.5 inches, the rear diameter 0.6 inches, creating a slight increase in wedge angle over the 1.35 inch body length. For the validation case, experimental and numerical models match in all dimensions. Observation of the figure shows the geometry of the numerical model and 3-D printed replica of the model used during the experimental investigation.

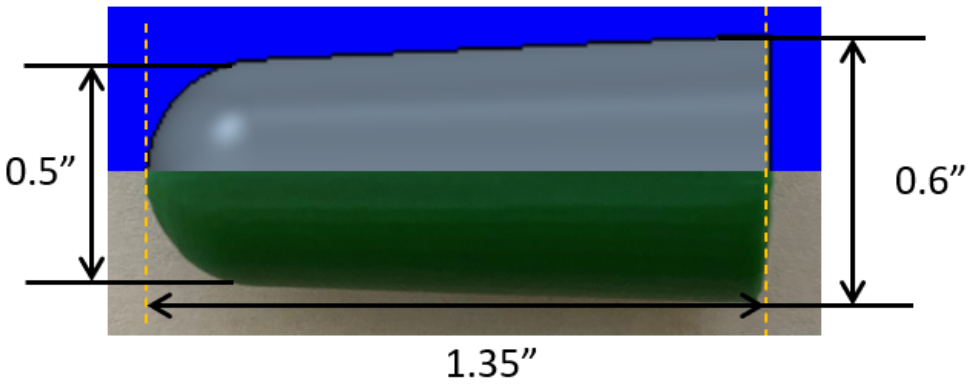

Figure 4.3: Model Geometry used for Experimental Results and Numerical Validation

4.4 Mesh Continua

Once the simulation domain is set, a mesh must be constructed to discretize the domain for surfaces and volumes, ultimately forming the mesh used to solve a numerical solution. This is considered a continuum in that the mesh is composed different models that discretize user defined regions differently. In this study the automated mesh option in Star CCM was used. User input parts are assigned to regions; these regions are then used to change the mesh criteria accordingly throughout the continuum to the users discretion. For each region, the users is able to adjust the values for default controls of the meshing models chosen and set specific custom controls for each region. In this study, surface, volume and prismatic boundary layer mesher were used to construct the mesh continua. Work done by P.G. Cross and M.R. West [3] show there are several viable options for determining automated mesh refinement criteria for automated refinement of the volume mesher. All cases conducted in this study make use of cell refinement based off normalized pressure gradient. Options for

refinement are explained and used as a supplement the structured refinement of the volumetric custom controls.

Structured Mesh

Before the adaptive mesh can be applied, a structured baseline mesh must be constructed consisting of the base surface, volume and prism cell meshes. The volume mesh is course in nature. However, the surface mesh is the basis for determining the aspect ration of the prism layer mesh used to accurately capture the viscous boundary layer. Significant refinement of the volume mesh is imperative in that it details the angle of the mach wave and detachment distance bow shock to the leading edge of the geometry, which is used for validation of the numerical results. To construct the full structured mesh, two volumetric controls, one surface control and one curve control are used, in addition to the default controls. The base size is set to 3mm with the each of the custom controls being designated as a percentage of the base size.

Setting	**Value**
Core volume mesh	Polyhedral mesher
Surface mesher	Surface remesher
Boundary layer mesher	Prism layer mesher
Base Size	3 mm
Number of prism layers	60
Prism layer near wall thickness	2.0e-8 mm
Prism layer total thickness	25% of base

Table 4.1: Default Mesh criteria for Base Mesh

Table 4.2 gives the values used to generate the default mesh shown in figure 4.4. The figure clearly shows the large gradient in cell size between the prism layer mesher and the base polyhedral volume mesh.

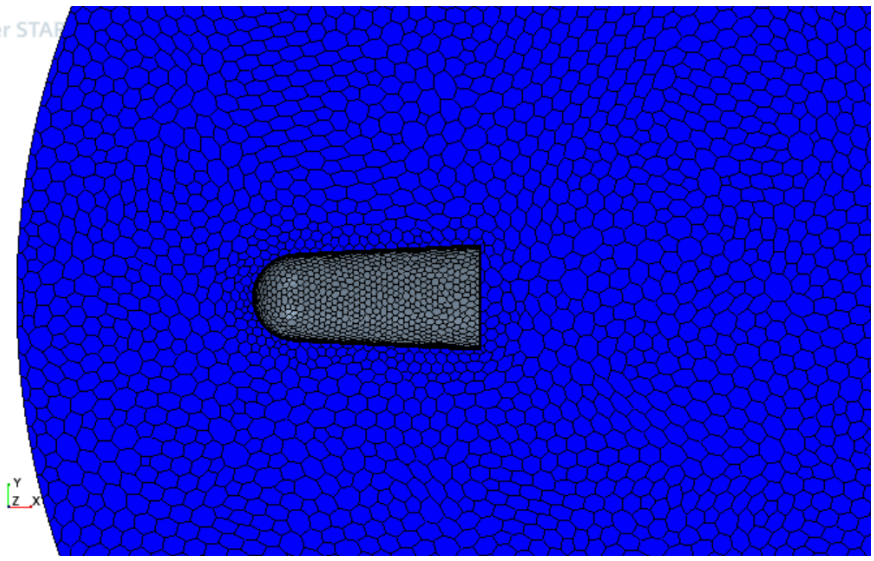

Figure 4.4: Default Mesh With No Custom Controls Assigned

Volumetric Controls

Volumetric controls were used to ensure the structured mesh is refined in areas where pressure and temperature gradients will be largest refine the mesh in regions of large velocity gradient. This also serves as a means to aid in solution convergence, accuracy, and as a supplement to automated mesh refinement. Two volumetric controls were set, the near and far geometries. The purpose of the near geometry was to ensure mesh fidelity in the volume closest to the geometry, where the largest gradients in the free stream properties are present. For this reason, the near control introduces mesh that is 20% of the 3mm base size, shown in figure 4.5. Also shown in the figure (4.5) is a second volumetric control, in the shape of a cone that encompasses a larger volume around the geometry; this secondary volumetric control is used to refine the mesh to 40% of the base size and capture the region of the flow regime that we see large pressure and density gradients from the presence of strong oblique shock waves.

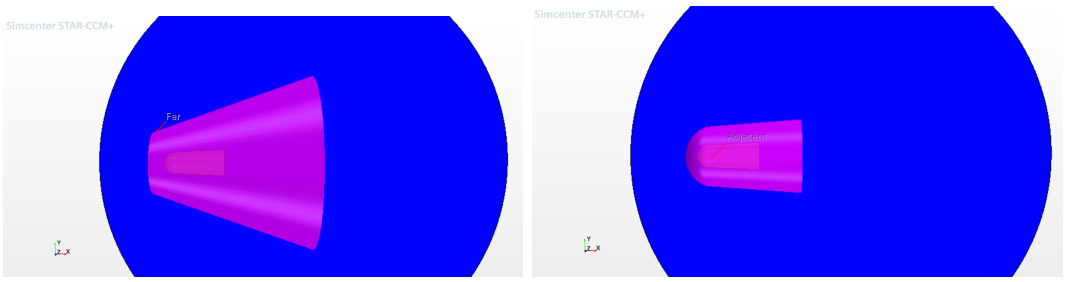

Figure 4.5: From Left to right: Geometry of the Far Field and Near Field Volumetric Controls.

Surface Controls

To control to the mesh at the surface of the geometry an additional meshing control was used. Application of a surface control to the surface of the geometry allows for control over the target and minimum surface size of the mesh. For this case mesh size was set to a percentage of the base size defined in the default controls of the mesh. For the validation case and all subsequent cases the surface mesh was given a 50% percent of base target size with a minimum possible size of 10% of the base mesh size. Volumetric and surface controls used in the simulations are tabulated in table 4.2.

Custom Control	**Value**
Near Geometry volume mesh	10% of base
Far geometry volume mesh	40% of base
Surface Control of geometry surface	50% of base

Table 4.2: Custom Meshing Control Size Summary

The final mesh used for the validation case is shown in fig 4.6. Observation of the figure shows the areas of increased refinement for both the near and far volumetric controls and the surface mesh refinement.

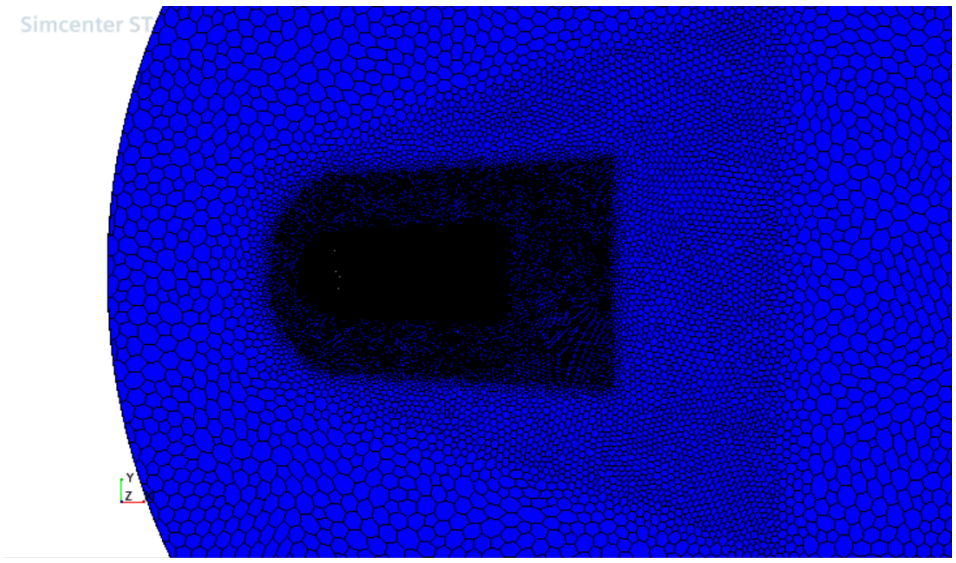

Figure 4.6: Complete Structured Mesh with Custom Controls Applied.

Automated Mesh Refinement

Automated Mesh Refinement is a physics option in Star CCM for users simulating in a 3-D domain. This refinement technique can also be accomplished in a 2-D simulations by means of user defined field functions. There are several common practices for automating mesh refinement. However, previous work on this topic shows that a user defined normalized pressure gradient field function is the preferred method for developing a refinement criteria [3]. Equation 4.7 shows the refinement function used in this work. With the pressure gradient is normalized, each cell has a value between zero and one. The range of refinement was set to 0.08-0.3. Physically, this function ensures that the ratio of the local cell size is smaller than the local length scale over which local pressure undergoes significant variation.

$$mag(grad(\$AbsolutePressure)) * \$AdaptionCellSize/(\$AbsolutePressure) \quad (4.7)$$

With a defined function for refinement, the user is prompted to determine the appropriate refinement criteria. Refinement criteria will determine which cells are coarsened or refined, minimum refinement size, refinement level, and the range in

which that refinement occurs. Table 4.3 gives the refinement criteria chosen for the automated mesh refinement applied for the validation case. The mesh convergence study conducted for the validation case defines the preferred adaption range for the cases.

Refinement Criteria	**Value**
Minimum Cell size	1.0e-7mm
Maximum Refinement Level	3
Adaption Method	User defined field function
Adaption Range	Coarsen< 0.08 >Keep< 0.3 <Refine

Table 4.3: Automated Mesh Refinement Criteria.

Each cell has a value between zero and one within the normalized pressure gradient. The refinement criteria defines which cells will be refined, coarsen or kept the same size. At each iteration frequency the process is repeated until the cells converge on the refinement range set by the user. Minimum cell size was determined by the prism layer mesher settings. Figure 4.7 shows the mesh at 2 and 10 refinement levels with the cell count annotated on the figure. As the solution converges the cells begin to refine further in the areas of highest pressure gradient.

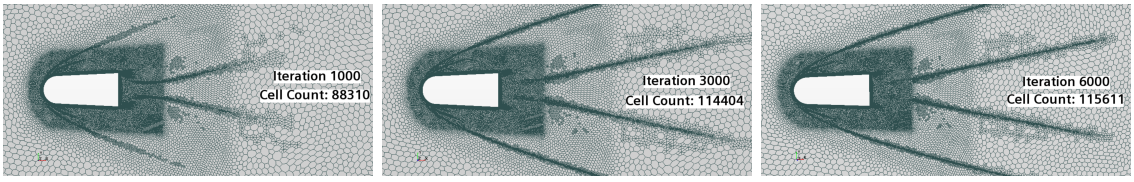

Figure 4.7: Automated Mesh Refinement at 1000, 3000 and 6000 Iterations Rectively

Mesh Convergence Study

To determine the preferred minimum cell size for automated mesh refinement a mesh convergence study was conducted for three different minimum cell sizes and three different mesh refinement ranges. Beginning with a larger minimum cell size and

refinement range, then decreasing in size. Net drag force vs. cell count for each case was recorded and plotted to determine when the solution had converged. Once the solution has converged the last 100 drag values were averaged and tabulated to determine when reducing the refinement no longer had a significant, less than 1%, change in the net drag value. The same process was completed for peak boundary heat flux.

Level	**Range**	**Net Drag (N)**
1	0.1<Keep>0.5	31.5
2	0.1<Keep>0.3	30.5
3	0.08<Keep>0.3	30.2
4	0.08<Keep>0.25	30.1

Table 4.4: Refinement Criteria for Automated Mesh Refinement.

Figure 4.8 shows the reports plot for net drag force and cell count. Observation of the figure shows the cell count monitor and drag force monitor beginning to converge around 5000 iterations. Although the cell count monitor is still slightly increasing as it continues to refine cells to the minimum cell size we see the net drag force is unchanged, thus resulting in a conclusion the mesh has fully converged.

Figure 4.8: Reports Plot Indicating Convergence of Automated Mesh

4.5 Physics Methodology

Physics settings and initial conditions for the validation case were set up to mimic the conditions present in the hypersonic wind tunnel. The Star CCM+ physics nodes and thier chosen settings for the validation case is given in table 4.5. In addition to the basic physics settings chosen for the numerical solution, specific changes were made to the material properties of air to match the properties of air present during the experimental tests that are more appropriate for modelling compressible flows. As mentioned previously, the Menter-SST version of the K-Omega turbulence model were used for the validation case and all other simulations. Turbulent viscosity ratio and intensity were adjusted to match that of recommendations from by P.G. Cross and M.R. West [3].

Node	Setting
Space	Three Dimensional
Time	Steady
Material	Gas
Flow	Coupled Flow
Equation of State	Ideal Gas
Viscous Regime	Turbulent
Reynolds Averaged Turbulence	K-Omega Menter-SST Turbulence Model
Optional Methods	Adaptive Mesh
Optional Methods	Cell Quality Remediation

Table 4.5: Physics Settings for the Validation Case.

Specific conditions for the material properties of air were changed from the default values. Dynamic viscosity of air was changed to follow Sutherland's law with a reference value of 1.717E-5 Pa-s and a Sutherland's constant of 198.6R. The Reference temperature for Sutherlands law used was 491.6R. Specific heats were modelled as a polynomial in temperature. Thermal conductivity of air was modelled using Sutherlands law as well with the reference value, constant and reference temperature the same as that of the dynamic viscosity. For air, the turbulent Prandtl number was set to a constant value of 0.9.

4.6 Solver settings

Certain settings within the solvers node were changed from their default setting to encourage solution convergence. First, the Expert driver CFL control method was selected. This method allows the user to specify an initial and target CFL number, and define a target number of AMG cycles. Within the Coupled implicit solver, adjustments were made to the Algebraic Multi grid (AMG) linear solver. The AMG

linear solver is employed to reduce convergence time by solving the underlying PDE's on a coarser mesh then applying that to the finer mesh to get a more accurate guess to the iterative solver and thus less residuals and faster convergence. The manner is which the AMG solver cycles through this process from coarse to finer grid is referred to as the cycle type. Changing the cycle type from a V cylce to an F cycle allows for more coarse level sweeps; while adjusting the Pre-sweep, post-sweep and max levels to 0, 2 and 3 respectively; this allows for pre-conditioning before the coarse level cycle is conducted. Additionally, positive results were yielded from using the MUSCL 3rd order discretization method and AUSM+ FVC coupled implicit flux method.

Setting	**Property**	**Method**
Coupled Implicit	CFL Control Method	Expert Driver
Expert Driver CFL	Target CFL	1
	Initial CFL	2.5
	Target AMG Cycles	8
AMG Linear Solver	Cycle type	F cycle
	Pre-Sweeps	0
	Post-Sweeps	3
	Max Levels	2
Convergence Accelerator	Continuity Convergence	AMG Linear Solver
Expert Initialization	Grid Sequencing	CFL Number: 2.5

Table 4.6: Solver Settings Used in The Validation and All Concurrent Cases.

The strategy for adjusting solver settings was based based on strategies developed by P.G. Cross and colleagues [3], including solution initialization settings and convergence accelerator settings. The validation case was ran with no macros in place although this is a viable option for complex geometries that are not converging and experiencing floating point exceptions. Table 4.6 lays out these settings and the

specific settings chosen for the solver settings used for simulations within this study.

4.7 Validation Results

The numerical solution was validated through physical comparison to schlieren imaging obtained from experiments on the UNCC hypersonic wind tunnel. To meet criteria for sufficient validation of numerical results, characteristics of the fluid in the numerical solution were kept consistent with experimental results. Initial conditions from the experiment show Mach 4.5 was achieved for the no cavity baseline case. Therefore, the numerical solution was done using the same mach number, free stream density, pressure and temperature as that of the experimental reference values shown in table. 4.7.

For a robust validation a numerical schlieren imaging function was used which is essentially the density gradient of the flow normalized and then applied to a half grey scale with an increased number of levels on the color map to allow for more refinement in areas where there is a large density gradient over a smaller region.

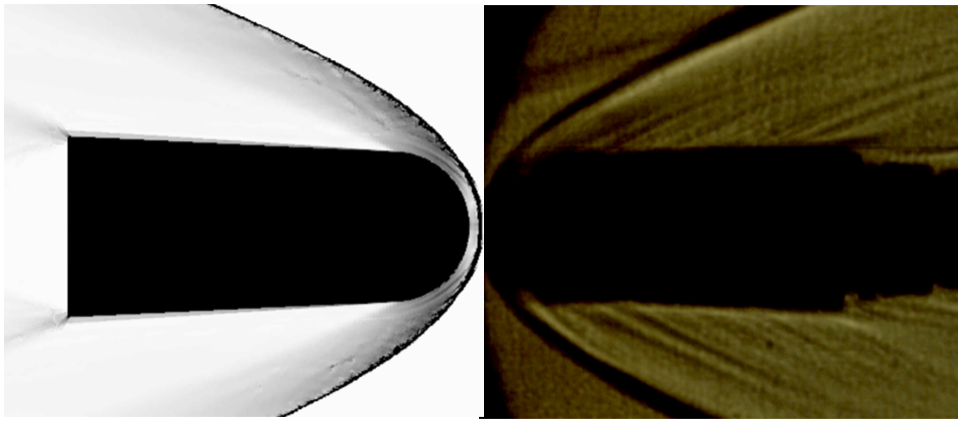

Figure 4.9: Numerical Schlieren Imaging vs. Experimental Schlieren Imaging

Results from the experimental imaging show the numerical and experimental imaging share the same density gradients, especially at the shoulder of the leading edge. The mach angle, and secondary shocks are consistent between both schlieren imaging

cases.

Table 4.7: Experimental and Numerical Reference Values

Value	**Simulation**	**Experiment**
Reference Pressure (Pa)	101325	101325
Fluid Density (kg/m^3)	1.20	1.20
Steady State Mach Number	4.5	4.5
Reference Temperature (K)	300	295

Further comparison of numerical results to experimental schlieren imaging was done by using an object detection machine learning code to investigate parts of the experimental flow regime and compare those results to the numerical schlieren imaging. In this case the same numerical schlieren function was used but the gray scale was changed to better match the color of the experimental schlieren results.A side by side comparison of numerical schlieren imaging to the refined experimental schlieren imaging results are shown in figure 4.10. This comparison allows for observation of the density gradients further down stream and a better analysis of the shock detachment distance that is more easily seen with the imaging code applied.

Figure 4.10: Numerical Schlieren Imaging vs. Experimental Schlieren Imaging

These results clearly show the mach wave angle and shock detachment distance

are approximately equivalent between experimental and numerical results. Density gradients at shoulder of the geometry do disrupt the view of the mach wave and its detachment distance. However, we are able to see the shape, angle and thickness of the mach wave match between the numerical and experimental case.

To ensure the prism layer mesher for the validation case was sufficient for use in other simulations that will be solving for heat transfer in turbulent cases, it was imperative to check the wall y+ was below 1. Figure 4.11 shows the y+ scalar distribution in Star CCM+. We see the y+ value is well below 1 for all of the surface area. We do see the y+ spike around the stagnation point. This is to be expected as it is the location of highest local Reynolds across the geometry. Several other cases were run in the mesh convergence study with prism layer near wall thickness at being an order of magnitude smaller. It was found that refining the first prism layer height further than 2.0e-8 had no significant impact on the y+ value.

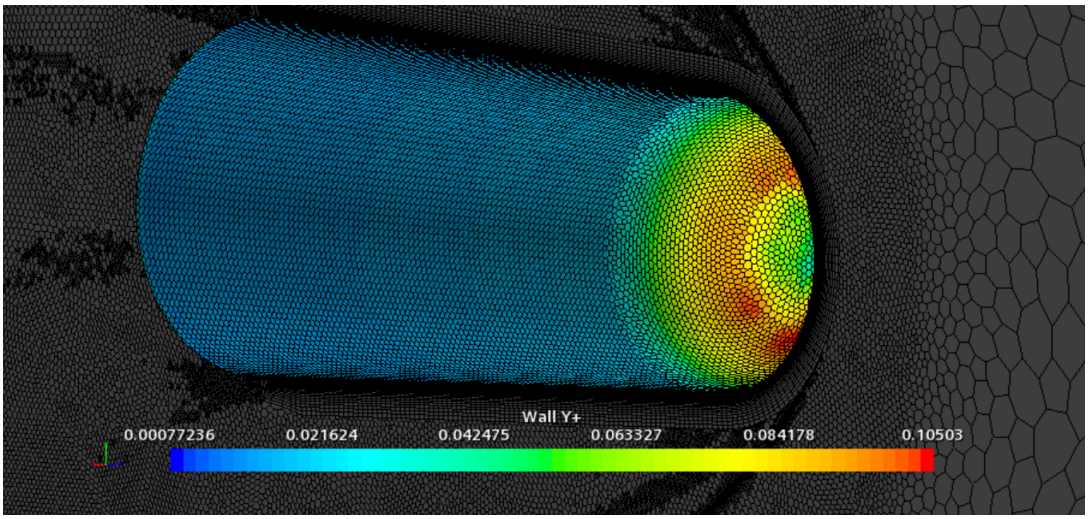

Figure 4.11: Scalar y+ of Validation Case

CHAPTER 5: RESULTS

5.1 Introduction

Results for the cavity and no cavity cases are examined for the boundary heat flux across the surface of the geometry and inside the cavity. Temperature and Mach number distributions are examined in depth for both the baseline and forward facing cavity cases. For heat transfer analysis of the forward facing cavity's effectiveness, a scalar distribution of the boundary heat flux for the cavity and no cavity case is compared. This is done for each of the three equations of state being examined. Additionally, a vector velocity distribution for each forward facing cavity is observed to better understand how the different equations of state effect vorticity distributions inside the cavity and its effect on the shock detachment distance. Convergence for each case is determined by examining the cell count vs net drag. As seen in the validation case, this method is sufficient for determining when a simulation has converged on a set range of refinement for the automated mesh. Refinement range was set to that of the validation case. All default and custom mesh controls were scaled accordingly to match the mesh continua from the validation case. Geometry for the cavity case is shown in figure 5.1.

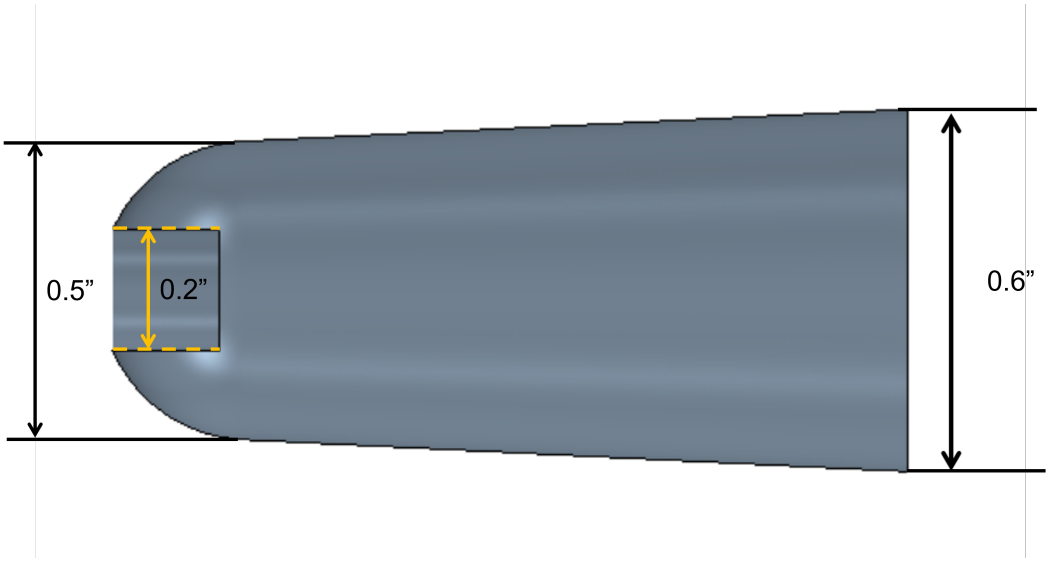

Figure 5.1: Forward Facing Cavity Geometry

Cavity length to diameter ratio of 1 was chosen for all the cavity simulations, with the diameter and depth of the cavity both being 0.2 inches. Overall length and outer diameter of the forward facing cavity geometry is consistent with the baseline no cavity geometry used in the validation case. This was done so meshing and solver settings could be used on the forward facing cavity case and provide consistency across simulations. Figure 5.2 shows a mesh distribution of the forward facing cavity, close observation of the figure shows where the curve control at the leading edge if the cavity creates a finer mesh, allowing for more resolution of the results in the areas where temperature and pressure will be highest. A supplemental volume control was used to refine the surface mesher with the region of the cavity. This allows for better results in the area where temperature and velocity gradients will be highest.

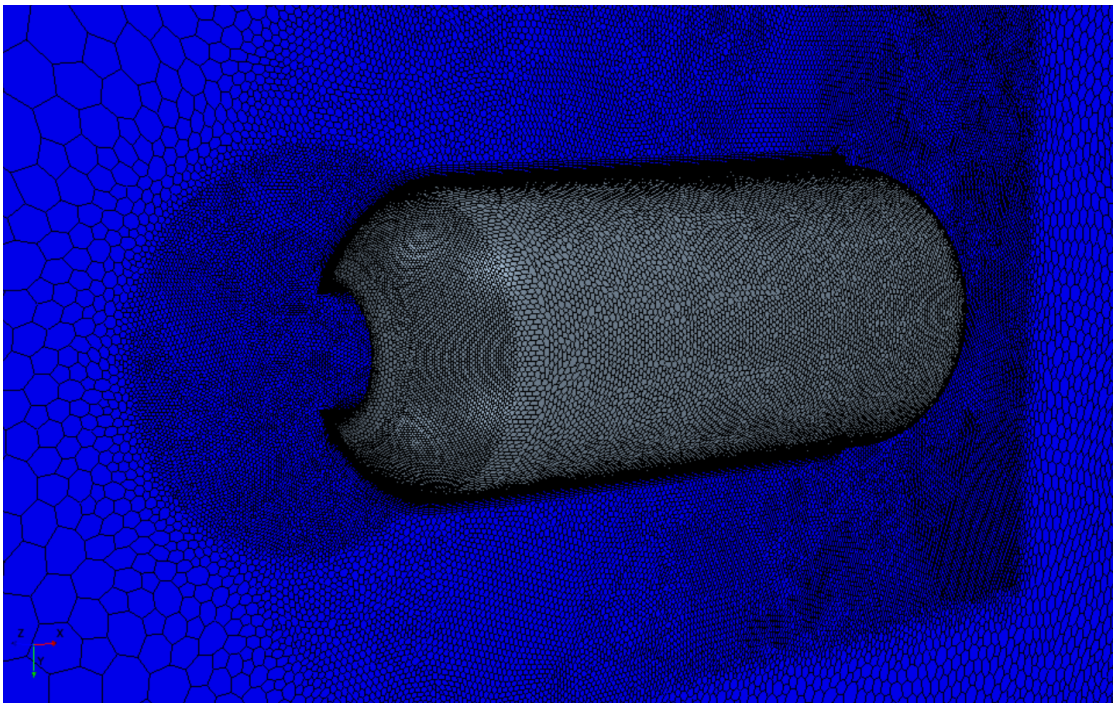

Figure 5.2: Forward Facing Cavity Geometry

To improve mesh fidelity at the leading edge of the cavity, a custom curve control was implemented at 2% of the base size, this can be observed in the figure. Automated mesh refinement and refinement criteria were kept consistent to the validation case.

5.2 Experimental Results

Experimental results obtained from schlieren imaging are presented for both cases. Further examination of the fully developed flow regime is performed with the application of an object detection machine learning code. The tool allows for variations in the image grey scale, which refines regions of the flow not clearly seen in the original schlieren imaging. Experimental results clearly show that the presence of the forward facing cavity weakens development of a fully formed shock wave, while strengthening the large density gradient at the leading edge of the test piece.

No Cavity Case

Results from the no cavity case show a mature shock wave developed in mach 4.5 free stream flow. A series of schlieren images were recorded over a time interval of 5 seconds, with the incoming flow reaching a steady state mach number of 4.5 for approximately 1.5 seconds, as shown in 5.5. Schlieren imaging obtained from the wind tunnel shows a pronounced shock wave consistent with that of a mach 4.5 free stream velocity. Large density gradients can be observed around the shoulder of the geometry, and further down the geometry, secondary shocks are present.

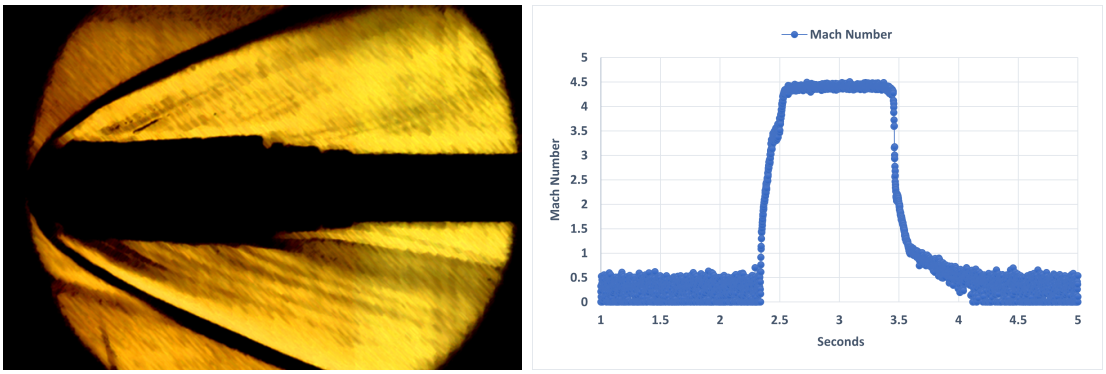

Figure 5.3: Numerical Schlieren Imaging and Mach Number Data From the Baseline No Cavity Experimental Case.

Cavity Case

Under the same conditions on hypersonic wind tunnel results from the cavity case are observed in the initial schlieren images and data from the experiment, shown in figure 5.4. Several runs on the cavity case were conducted, each yielding the same results of a steady state Mach 3.5 free stream velocity. This is likely due to placement of the pressure sensor inside the test chamber. Investigation of the schlieren imaging of the experiments supports the effectiveness of the cavity in that the mach angle for the cavity case is at a much larger angle than the the baseline no cavity case. We also see the bow shock has moved further forward of the cavity.

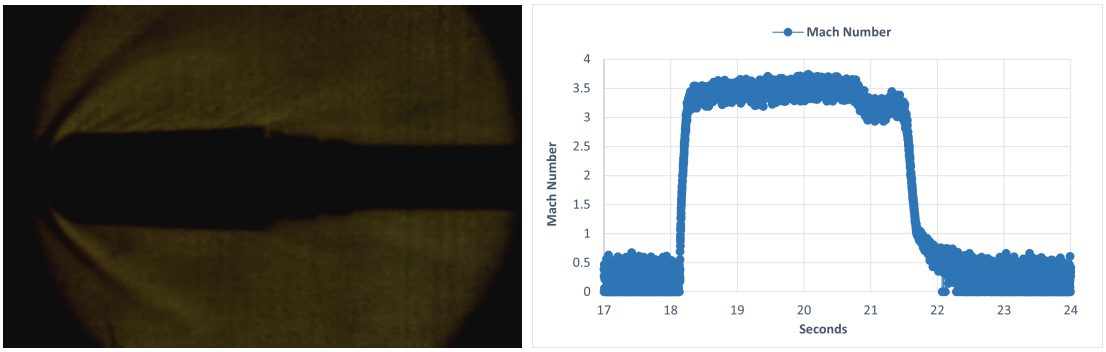

Figure 5.4: Numerical Schlieren Imaging and Mach Number Data From the Cavity Experimental Case.

5.2.1 Visualizing Results Using Activity Detection

Further analysis of the experimental results was performed using an object detection machine learning code. This allows for the gradient of the gray scale to be refined from the original imagining and allows for the examination of the mach wave and flow regime characteristics that can not been seen in the original schlieren imaging. The imagining code was originally used as an object detection code. It's application to the schlieren imaging changes the gray in such a way that the pixels that are changing from one photo to another are black and the areas of the flow regime that are not changing stay white. This allows for a unique perspective of the flow regime, especially in a transient case. The code functions as such: The images are converted to gray scale, then a time series matrix is created from the gray scale image. Next, an SVD matrix is computed from the time series matrix and given a rank k approximation. Then finally, the low rank matrix is subtracted from the original matrix to give the viewed image [16]. Two different k values were used to investigate the flow regime of the cavity and non-cavity cases. Each case was examined using a k value of 1 and a k value of 20. Figure 5.5 shows the no cavity case for the k values of 1 and 20.

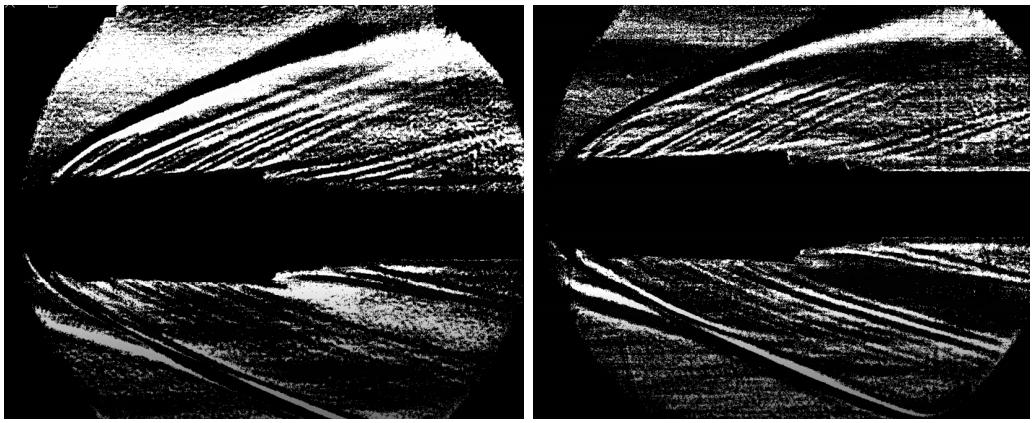

Figure 5.5: From Left to Right: Schlieren Imaging With a Low Rank Flow of 1 and 20 Respectively for the No Cavity Case at Mach 4.5

Results from the no cavity case show more pronounced secondary shocks than seen in the original schlieren imaging. The k rank of 1 image also shows the secondary shocks are present much closer to the shoulder of the test piece than in the k rank of 20 or in the original schlieren imaging. Another interesting observation is how well defined the leading shock is for the k rank of 20 case in comparison to the original imagery and the k rank 1 images.

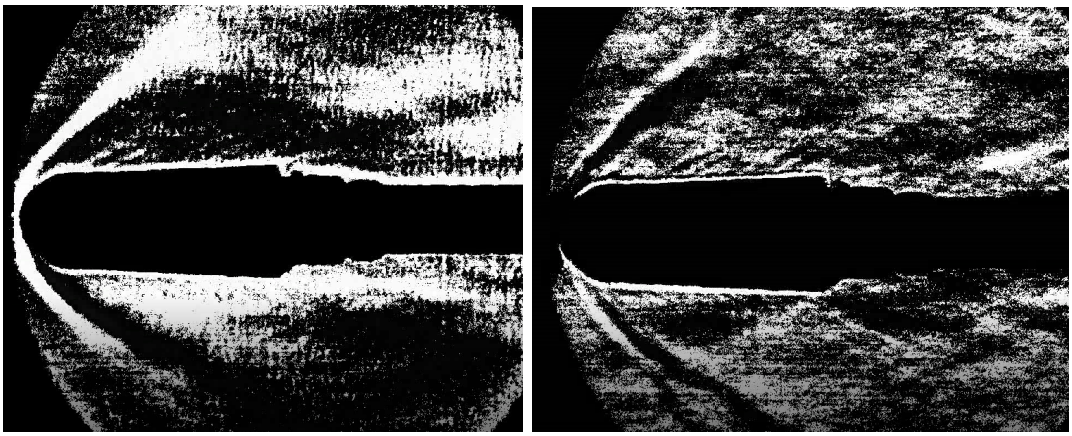

Figure 5.6: From Left to Right: Schlieren Imaging With a Low Rank Flow of 1 and 20 Respectively for the Cavity Case at Mach 3.75

Observation of the cavity case images show the same trend as the no cavity cases, but slightly magnified. Some secondary shocks that were not present in the original schlieren imaging are present in the investigated images, this is especially true for

the higher ranking k approximations. This is due to the algorithm capturing the parts of the images that are changing from one frame to the next; allowing us to see more minute characteristics of the flow regime than are seen in the original schlieren imaging.

5.3 Computational Results

Numerical results for the cavity and no cavity cases were examined for temperature distribution and boundary heat flux to determine the cavity's effectiveness in decreasing heat transfer at the surface of the geometry, most importantly the leading edge where the heat flux is at its maximum. The present study focused on the equation of state and its effect on the magnitude of heat transferred. First, an examination of the shock detachment distance for each equation of state was carried out to understand the significance the equation of state has on the density gradient behind the leading bow shock. Then, an examination of the equation of state's affect on net drag is carried out. Finally, notable differences in the numerical solution at the stagnation point are observed, depending on equation of state used.

Mach wave distributions for each equation of state are displayed in figures A.6 through 5.9. Results show the thermal equilibrium (Real Gas) case has the most pronounced effect on shock detachment distance, followed by the two species thermal non-equilibrium cases, then the ideal gas case. Results also show that the ideal gas law case underestimates the circulation inside the cavity compared to the other results. This is consistent with how it handles the stagnation point of the no cavity case as well.

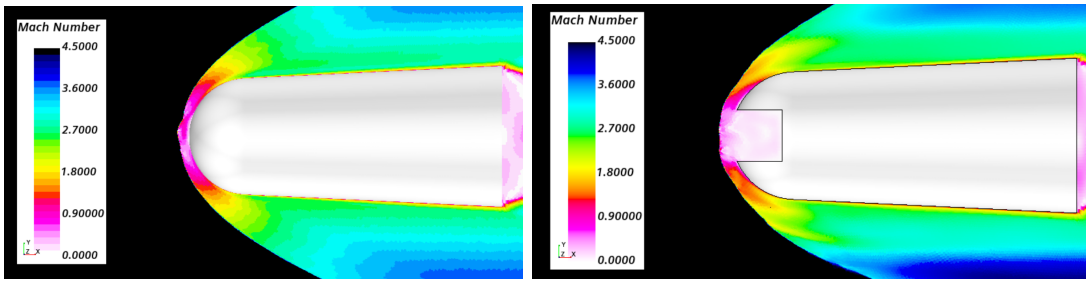

Figure 5.7: Mach Distribution Of the Cavity and No Cavity Case for the Ideal Gas Equation of State.

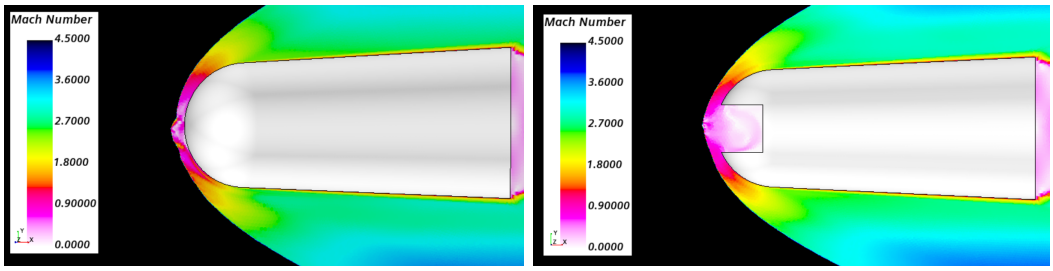

Figure 5.8: Mach Distribution Of the Cavity and No Cavity Case for the Real Gas Equation of State.

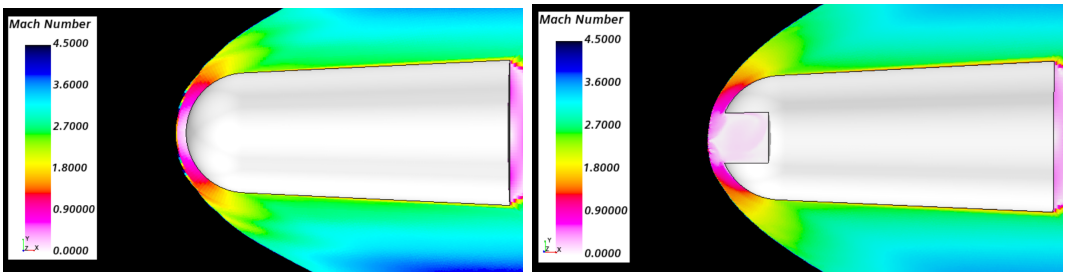

Figure 5.9: Mach Distribution Of the Cavity and No Cavity Case for the Two Species Thermal Non-Equilibrium Equation of State.

Convergence was very consistent among the simulations. All the cavity cases began converging to solution at 6000 iterations initially, and no cavity solutions around 5000 iterations. All cavity simulations were set to stopping criteria of 6000 iterations, and all cavity cases to 8000 iterations. The CFL number was kept at 1 for all cases. Once the initial stopping criteria was reached, the simulations were checked for convergence and then run further if needed. In general, the cavity simulations take an extra 1000 iterations to reach convergence vs the no cavity simulations. Two species thermal

non-equilibrium cases are the most computationally expensive of the cases ran, but proved to be the most stable. Once converged, the simulations were first examined for mach number distributions, and the shock detachment distance from the leading edge was measured in Star CCM+. For each of the six cases examined, table 5.1 gives shock detachment distance with respect to each equation of state, for both the cavity and no cavity cases.

Geometry	**Equation of State**	**Shock Detachment Distance (mm)**
No Cavity	Ideal Gas	0.9
	Real Gas	1.0
	Thermal Non-Equilibrium	1.1
Cavity	Ideal Gas	1.1
	Real Gas	1.2
	Thermal Non-Equilibrium	1.5

Table 5.1: Shock Detachment Distance of Cavity and No Cavity Case for Each Equation of State.

Net drag on the body is then determined by averaging the last 100 values from the drag force monitor used to determine convergence. Analysis of the results pose an interesting trend between shock detachment distance and net drag. Correlation between shock detachment distance and net drag is represented in table 5.2. Results show that net drag on the body increases with shock detachment distance. Although it is a small sample size of results, there is an almost linear relationship between the two values. We see that the thermal equilibrium case creates the largest shock detachment distance and the largest net drag; an 11% increase in net drag compared to the Real Gas case, and an almost 22% increase compared to the Ideal gas case with the introduction of the cavity .

Geometry	**Equation of State**	**Net Drag (N)**
No Cavity	Ideal Gas	32.5
	Real Gas	33.1
	Thermal Non-Equilibrium	32.9
Cavity	Ideal Gas	31.8
	Real Gas	35.7
	Thermal Non-Equilibrium	39.3

Table 5.2: Net Drag Of Cavity and No Cavity Case For Each Equation Of State.

Figure 5.10 shows the scalar temperature distributions for the cavity cases. Results show that the maximum temperature appears within the cavity and at the lip of the cavity. This is consistent with boundary heat flux results discussed later in the results section. Real gas and Ideal Gas equations of state show larger variations of temperature inside the cavity, relative to the thermal non-equilibrium model. The thermal non-equilibrium case predicts a maximum temperature value at the front of the cavity. Additionally, the real gas equation of state shows a much larger temperature gradient within the boundary layer.

Physically, we interpret these results in terms of the gas specific heat, c_p. In particular, specific heat measures/indicates the sum of the equilibrium molecular thermal (kinetic) and (intermolecular) potential energies extant within any given N-molecule gas fluid particle. In the ideal gas model, it is implicitly assumed that relaxation of molecular energy modes - specifically, translational, rotational, vibrational, and electronic - excited by passage of gas molecules through the bow shock, relax on time scales much shorter than the characteristic time, τ_{flow}, required for the molecule to travel from the downstream side of the shock to the test piece. By contrast, c_p for the real gas and two specie nonequilibrium models account, at two different levels of approximation, for the fact that molecular energy modes excited by flow through the

bow shock levels, relax on time scales that are likely on the order of, or greater than τ_{flow}. Thus, molecules in the real gas and two specie nonequilibrium models carry more of the thermal and potential energy modes excited by the bow shock to the work piece surface.

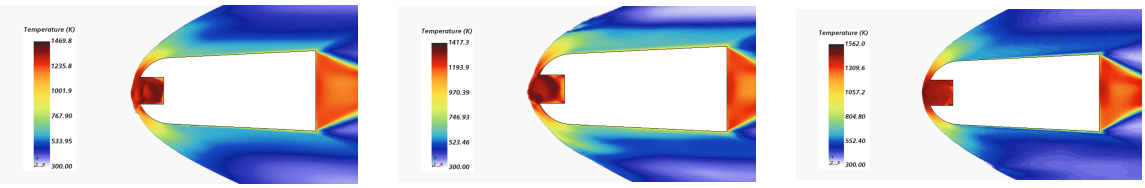

(a) Ideal gas (b) Real gas (c) Thermal non-equilibrium

Figure 5.10: Cavity Scalar Temperature Distributions

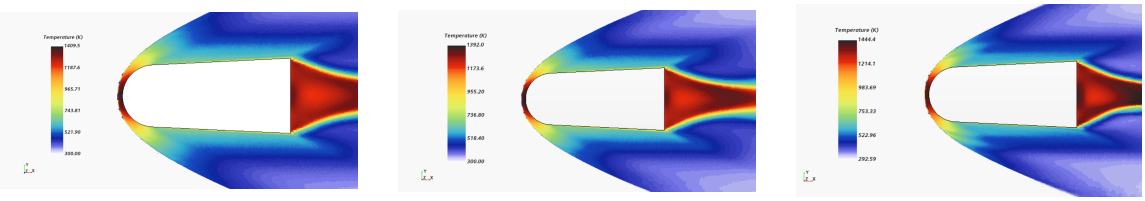

(a) Ideal gas (b) Real gas (c) Thermal non-equilibrium

Figure 5.11: No Cavity Scalar Temperature Distributions

5.3.1 Boundary Heat Flux

Boundary heat flux of each numerical case was computed by analyzing the heat flux across the surface of the geometry. This was computed for both no cavity and cavity cases, for each equation of state, in order to determine the magnitude of the heat flux at the leading edge of the geometry, as well as how heat flux decays downstream of the test piece shoulder.

No Cavity Case

Figure 5.12 gives a graphical representation of the boundary heat flux vs. axial position for the no cavity cases. Observation of the data presented in the figure shows that the two species thermal non-equilibrium case predicts a larger heat flux at the leading edge, relative to the ideal and real gas equation of state cases. Real gas and ideal gas equation of state models lead to the same trends, where the ideal gas model significantly under-predicts heat flux at the leading edge relative to the other models. The data clearly shows that all three models predict an initial spike in heat flux at the stagnation point, which then slightly decays before the laminar boundary layer transitions to turbulent, as manifested by the drastic increase in heat flux along the shoulder. The subsequent decay in boundary heating reflects decay of the turbulent boundary layer wall shear stress and associated decay in viscous (frictional) boundary layer heating. Results for axial positions are reported to the front half of the geometry since there are no changes in the heat flux further downstream.

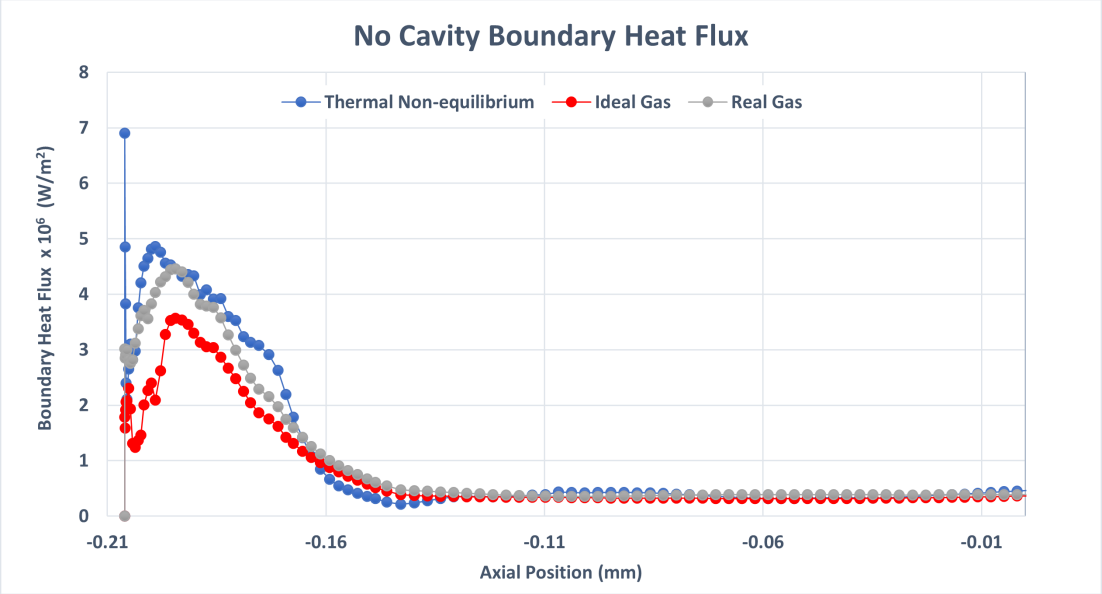

Figure 5.12: Boundary Heat Flux For Each Equation Of State On the Baseline No Cavity Case.

Boundary heat flux distributions for all three equations of state are shown in figure 5.13. The figure clearly shows how the heat flux is distributed across the shoulder of the leading radius. For reference, magnitude and distribution of the boundary heat flux is shown in all sub figures.

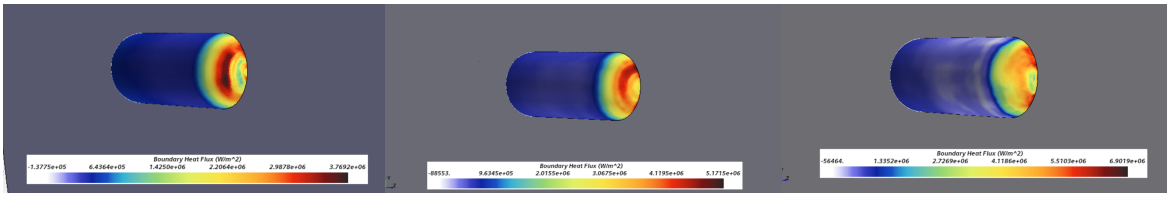

(a) Ideal Gas (b) Real Gas (c) Thermal non-equilibrium

Figure 5.13: Scalar Boundary Heat Flux Scenes For the Baseline No Cavity Cases.

As a check on the physical fidelity of the computed results, y+ distributions for each of the no cavity cases are shown in figure 5.14. Results show that y+ remained

below 1 for all cases, indicating that the meshing and prism layer approaches outlined in Chapter 4 are realistically capturing the complex flow physics in the near-surface boundary layer. All cases show a maximum y+ magnitude near the stagnation point, which then decreases drastically downstream of the shoulder.

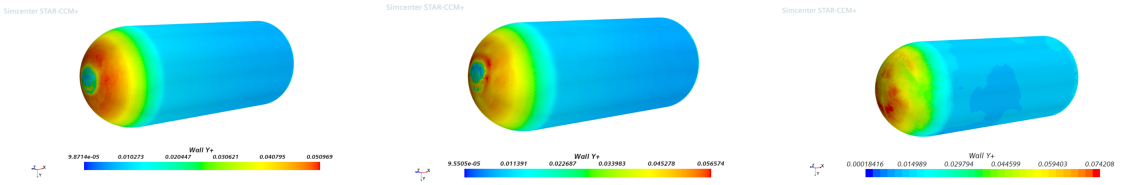

(a) Ideal Gas (b) Real Gas (c) Thermal non-equilibrium

Figure 5.14: Scalar y+ Scenes For the Baseline No Cavity Cases.

Cavity Case

For the cavity cases, boundary heat flux is graphed individually for clarity, and the heat flux inside and outside the cavity are examined. In order to separate the data between the external body profile and internal cavity, the data focus tool in Star CCM+ was used. Points in blue represent data inside the cavity, while data in red depict heat flux on the external profile. Cavity case simulations show similar trends to those observed in the no cavity case. The thermal non-equilibrium model again predicts the largest heat flux magnitude, this time inside the cavity. The ideal gas case predicts the largest heat flux on the external profile, relative to the other equations of state. For all three models, the largest heat flux is observed at the lip of the cavity on the external profile, then decays rapidly across the shoulder of the radius. Figure 5.15 show the boundary heat flux for the Ideal Gas model, 5.16 for the Real Gas (thermal equilibrium) model, and 5.17 for the two species thermal non-equilibrium model.

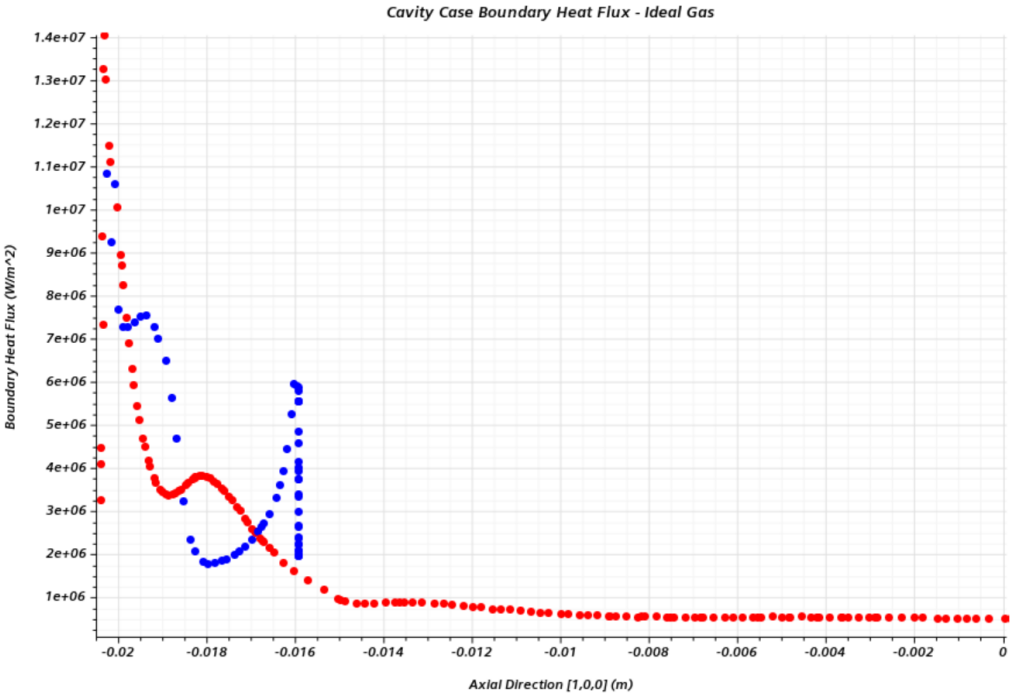

Figure 5.15: Boundary Heat Flux for Ideal Gas Equation Of State

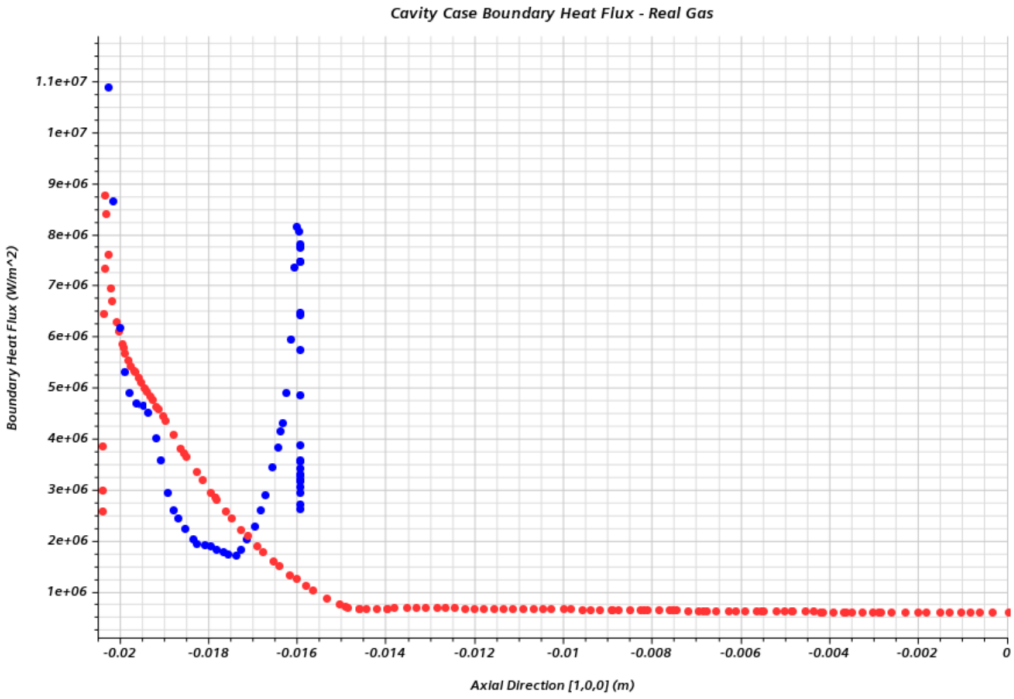

Figure 5.16: Boundary Heat Flux for Real Gas Equation Of State

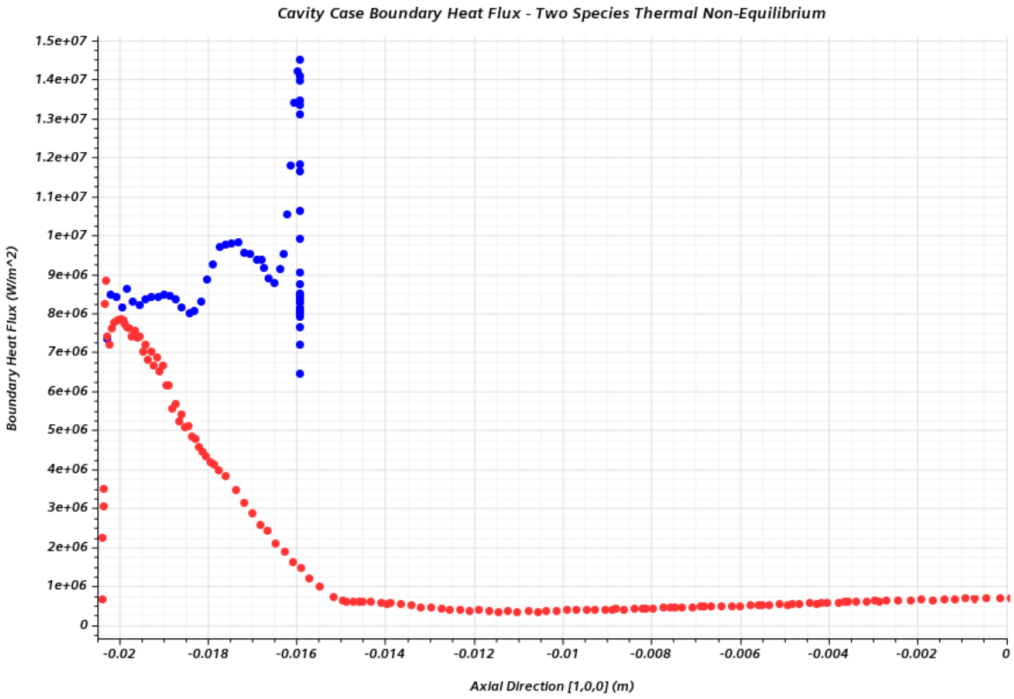

Figure 5.17: Boundary Heat Flux for the Two-Species Thermal Non-equilibrium Equation Of State

Comparing these results, it is extremely interesting that the the two-species nonequilibrium model indicates that, to within the spatial resolution of the numerical solution, no transition from a laminar to turbulent boundary layer takes place. At present, we don't have enough data to determine whether the boundary layer in this case is entirely turbulent, from the nose and all points downstream, or whether the boundary layer is wholly laminar, never transitioning. Although computed heat flux magnitudes are approximately an order of magnitude larger in the two-species non-equilibrium model, suggesting that the boundary layer is wholly turbulent, the large fluxes could be due to the fact that the gas is carrying more shock-induced thermal energy to the body surface. More work is required to answer this important question; a scaling analysis of the physical processes taking place in the two-species model will be reported in a future publication.

Boundary heat flux distributions are presented for the cavity cases in figure 5.18.

From the distributions, we see that the maximum heat flux occurs at the lip of the cavity. We also observe that the magnitude of the heat flux decays drastically before the shoulder of the radius. Overall, maximum heat flux magnitudes between the cavity and no cavity cases are similar. However, for the cavity cases, we observe that heat flux magnitudes decay rapidly following the initial spike. The no cavity cases see higher heat flux magnitudes sustained across the geometry, and especially at the shoulder of the radius.

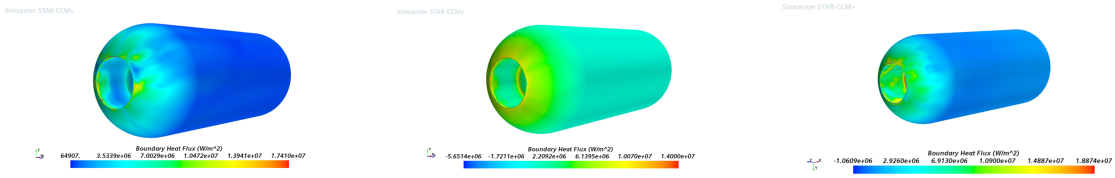

(a) Ideal gas (b) Real gas (c) Thermal non-equilibrium

Figure 5.18: Boundary Heat Flux Scalar Scenes For all Cavity Cases.

Again, y+ distributions are shown in figure 5.19. The maximum y+ occurs at the lip of the cavity and then decreases dramatically across the shoulder, consistent with the no cavity cases. In general, y+ is highest in areas where wall shear stress is highest, as to be expected. Another trend that was consistent with the no cavity case is the y+ being smallest for the ideal gas equation of state, showing that the computed wall shear stress is smaller for the ideal gas model. This feature, in turn, undoubtedly changes the predicted location for laminar to turbulent boundary layer transition.

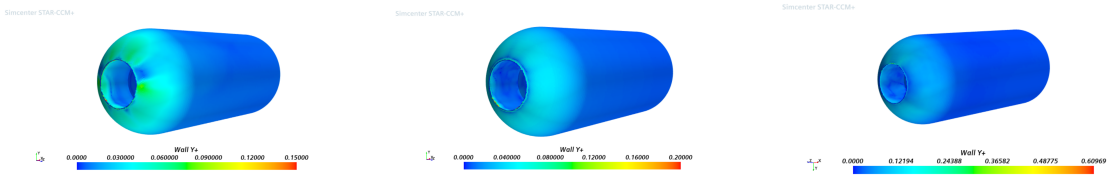

(a) Ideal gas (b) Real gas (c) Thermal non-equilibrium

Figure 5.19: y+ Scalar Scenes For all Cavity Cases.

Velocity vector distributions are shown below for each of the three gas models used. We see that calculated cavity velocity fields differ significantly for each gas model. Figure 5.20 shows two large areas of recirculating flow inside the cavity and the vorticity dissipating rapidly in front of the cavity. There are however two small regions of recirculating flow in front of the cavity just before the bow shock. Note that the distributions shown are instantaneous snap shots of computed flow fields; the asymmetry in computed cavity flows reflects the fact that due to excitation of in-cavity resonant modes, these flows are intrinsically unsteady.

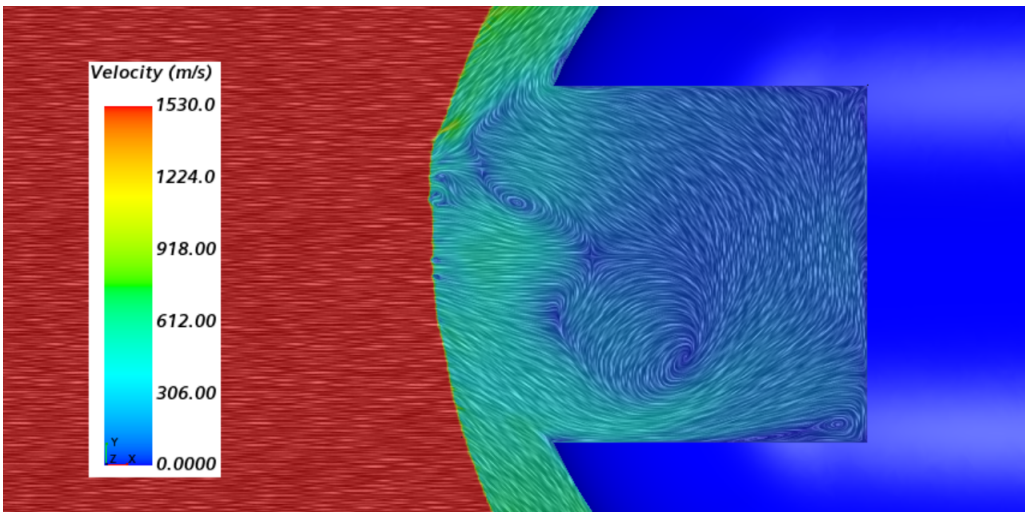

Figure 5.20: Ideal Gas Cavity Case Velocity Vector Distribution

The real gas model predicts the most vorticity inside the cavity, with four distinct areas of recirculation shown at the bottom of the cavity. Figure 5.21 shows that in front of the cavity, as in the ideal gas case, vorticity dissipates in a similar fashion. This is indicative of the high temperatures computed inside the cavity for the real gas case. The real gas model also predicts the smallest velocity magnitudes inside the cavity, relative to the other cases.

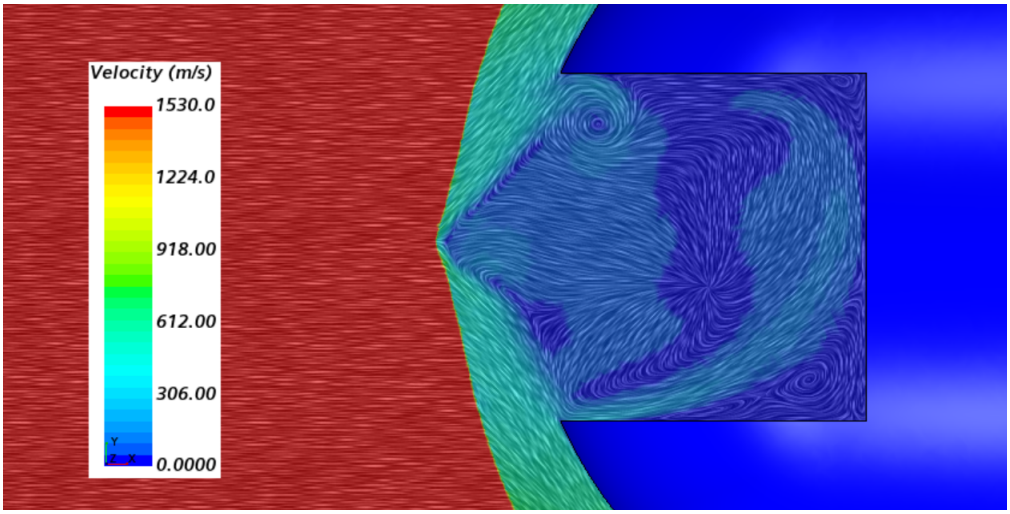

Figure 5.21: Real Gas cavity Case Velocity Vector Distribution

The two species thermal non-equilibrium model (figure 5.22 predicts two large areas of recirculation, as well as one large region slightly forward of the cavity. This flow structure provides a physical explanation for the larger shock detachment distance observed with this model. In essence, the larger vorticity inside the cavity and increased pressure gradient produce a virtual fluid surface that extends away from the actual surface, pushing the bow shock further from the test piece. Finally, for the thermal non-equilibrium case, we observe lower velocity magnitudes reaching all the way to the lip of the cavity. This is most likely due to the vibrational and rotational temperature differences computed for the two-species model.

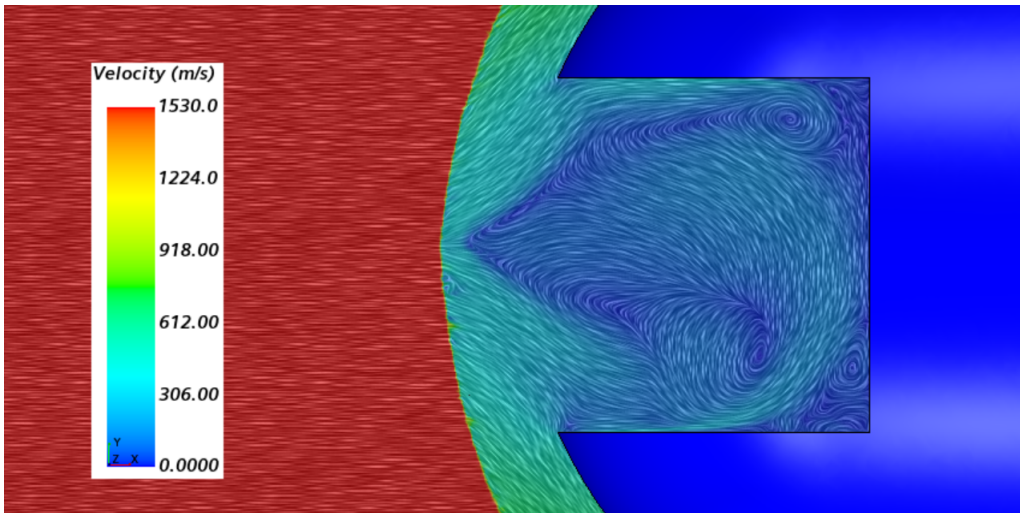

Figure 5.22: Two Species Thermal Non-equilibrium Gas Case Velocity Vector Distribution

5.3.2 Discussion of Results

Results from the numerical modeling show that the introduction of a cavity does decrease heat transfer at the leading edge of the vehicle. Observations of the experimental and numerical results shows that the introduction of the cavity results in low velocity, virtual fluid surfaces and increased pressure gradients that move the bow shock further forward of the leading edge, increasing shock detachment distance. This does come at some cost though, as the net drag also increases as the shock detachment distance increases. Although the overall heat transfer is less for the cavity case, the maximum heat flux computed at the lip of the cavity is greater than the maximum heat flux seen in the no cavity cases.

Results also demonstrate that numerical results are dependent on the gas equation of state used. Physically, the ideal gas model implicitly assumes fast relaxation of molecular energy modes excited by flow through the bow shock: Relaxation happens on time scales much shorter than the time required, τ_{flow}, for gas molecules to move from (the downstream side of) the bow shock to test piece surface. By contrast, the real gas equilibrium and two-species nonequilibrium models capture the fact that

molecular energy modes, excited by flow through the shock, relax on relatively long time scales. The numerical results strongly suggest that these relaxation times are on the order of, or greater than τ_{flow}.. We see this in figures 5.23 and 5.24. The vibrational electronic and rotational-translatioanl energy modes respectively. Real and Ideal Gas equations of state assume instant relaxation of the molecules as they pass through the leading shock wave. The thermal non-equilibrium case takes into account the relaxation time and thus we see much larger total energy inside the cavity that is transferred to the surface as heat. The vibrational-electronic temperature scene shows the areas of local heat flux maximum at the base of the cavity that are seen in the boundary heat flux graphs.

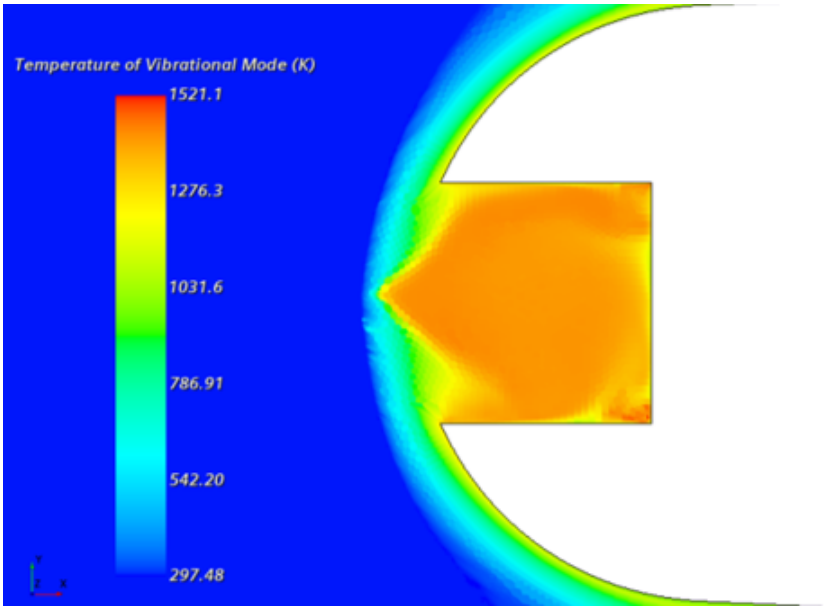

Figure 5.23: Vibrational-Electronic Temperature Scene for the Two Species Thermal Non-Equilibrium Case

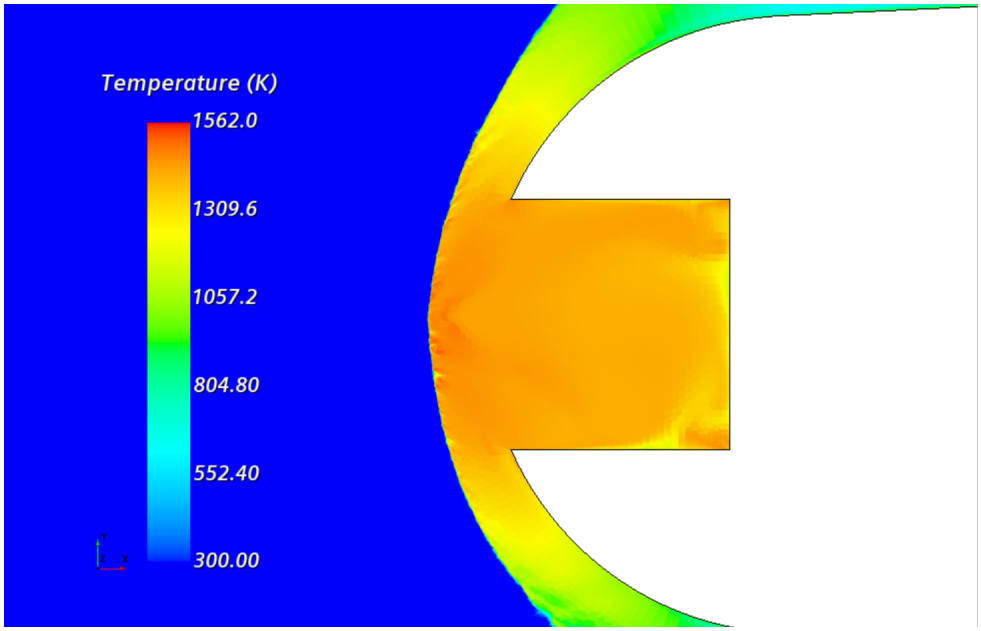

Figure 5.24: Translational-Rotational Temperature Scene for the Two Species Thermal Non-Equilibrium Case.

The ideal gas and real gas equations of state show very similar trends, for both the inviscid and viscous analysis, but with large discrepancies in the magnitude of heat transferred. The two species gas model also showed similar trends to the other gas models, but predicted significantly higher fluxes. An important question exposed in this study concerns whether nonequilibrium suppresses transition from laminar to turbulent boundary layer flow. Future work will focus on this question. Notable differences are observed in heat transfer magnitudes predicted by the three gas models. Again, we interpret the larger fluxes predicted by the real gas and two species models as reflecting significant transport of excited molecular energy modes from the bow shock to the test piece.

Finally, observation of figures 5.20,5.21 and 5.22 shows the clear relationship between re-circulation inside the cavity and shock detachment distance. We see that the lower velocity and higher pressure behavior inside the cavity results in pronounced bow shock movement forward of the leading edge.

CHAPTER 6: SUMMARY AND FUTURE WORK

Experimental and numerical analysis was done on a psuedo blunt body sbujected to a Mach 4.5 flow regime, with and without a forward facing cavity. The aim of this investigation was to first validate that the forward facing cavity increases shock detachment distance. Then through numerical simulation how the equation of state changes the inviscid and viscous results of the cavity introduction. Both the experimental and numerical results were run at a free stream Mach 4.5. Validation of numerical results was done through numerical schlieren imaging and schlieren imaging collected from the hypersonic wind tunnel. Physics, solver and mesh settings were validated through this case and then used in further investigations of viscous effects with the changing of the gas dynamics computation. The analysis of viscous effects was done using an Ideal gas law, Real Gas or thermal equilibrium, and a two species thermal non-equilibrium equation of state.

Mesh settings were consistent across all cases and were determined by mesh convergence study conducted during the validation case, evaluating the refinement range of the automated mesh refinement technique used. A baseline structured mesh was used to encourage early convergence, and a automated mesh refinement of the volume mesher was used to refine the regions of the flow regime with the largest pressure gradient. Convergence of each solution was determined by a net drag and cell count annotation, once these two values had converged then it was determined the mesh refinement was complete. Residuals of each case were also checked to ensure convergence of the numerical solution.

Experimental and numerical results show there is benefit to having a forward facing cavity at the stagnation point of the hypersonic body. The introduction of a cavity,

reduces overall heat transfer at the leading edge and moves the bow shock further forward of the body. However, transient effects and very high temperature effects that could lead unpredictable dynamic responses were not investigated in this work. There has also been an abundance of research conducted on cavity size, shape, and length to diameter ratio. For this thesis a generic cavity geometry was used to focus on the solver and physics settings for the numerical case and to focus on schlieren imaging setup and functionality of the hypersonic tunnel for the experimental case.

Future work should include various cavity geometry at higher Mach number to determine a more solidified relationship between cavity geometry and net drag. There should also be more investigation into the heat loads at the lip of the cavity. This area is inevitably more susceptible being that it is apparent higher friction loads will occur at the lip of the cavity. There should also be further work done on the multi-species numerical model. To better understand a more accurate numerical solution a reacting thermal non-equilibrium case should be conducted to best evaluate the heat loads on the leading edge of the cavity. This approach is also the most accurate for modelling boundary layer transition and the turbulent viscosity ratio. This is a much more computationally expensive approach. However, using the ideal gas law has shown to over predict the aerothermodynamics and heat transfer within the flow regime. Some consideration should be taken into simulating higher Mach numbers with a multi-species reacting gas model.

REFERENCES

[1] P. Bradshaw and G. P. Huang, "The law of the wall in turbulent flow," *Proceedings of the Royal Society of London. Series A: Mathematical and Physical Sciences*, vol. 451, no. 1941, pp. 165–188, 1995.

[2] S. Saravanan, G. Jagadeesh, and K. Reddy, "Investigation of missile-shaped body with forward-facing cavity at mach 8," *Journal of Spacecraft and Rockets*, vol. 46, no. 3, pp. 577–591, 2009.

[3] P. G. Cross and M. R. West, "Simulation of hypersonic flowfields using star-ccm+," tech. rep., Naval Air Warfare Center Weapons Division, 2019.

[4] W. S. L. C. of Engineering, "Hypersonic wind tunnel research," Apr 2021.

[5] M. White, "Improvement of optical and pressure sensing capabilities of the unc charlotte hypersonic wind tunnel," Master's thesis, The University of North Carolina at Charlotte, 2021.

[6] M. Netterfield, "Validation of a navier-stokes code for thermochemical non-equilibrium flows," in *27th Thermophysics Conference*, p. 2878, 1992.

[7] P. Siemens, "Star-ccm+ user guide version 13.04," *Siemens PLM Software Inc: Munich, Germany*, 2019.

[8] https://www.pointwise.com/yplus/index.html. Mesh Generation Software for CFD, "Compute grid spacing for a given y+."

[9] H. Bawangaonwala, "Nusselt number: Its important relations and formulas and 10 + faqs," May 2021.

[10] R. N. Gupta, K.-P. Lee, R. A. Thompson, and J. M. Yos, "Calculations and curve fits of thermodynamic and transport properties for equilibrium air to 30000 k," tech. rep., 1991.

[11] S. Saravanan, K. Nagashetty, G. M. Hegde, G. Jagadeesh, and K. P. J. Reddy, "Schlieren visualization of shock wave phenomena over a missile-shaped body at hypersonic mach numbers," *Proceedings of the Institution of Mechanical Engineers, Part G: Journal of Aerospace Engineering*, vol. 225, no. 1, pp. 26–34, 2011.

[12] Z.-g. Wang, X.-w. Sun, W. Huang, S.-b. Li, and L. Yan, "Experimental investigation on drag and heat flux reduction in supersonic/hypersonic flows: A survey," *Acta Astronautica*, vol. 129, pp. 95–110, 2016.

[13] B. Sudarshan and S. Saravanan, "Heat flux characteristics within and outside a forward facing cavity in a hypersonic flow," *Experimental Thermal and Fluid Science*, vol. 97, pp. 59–69, 2018.

[14] R. Yadav and U. Guven, "Aerodynamic heating of a hypersonic projectile with forward-facing ellipsoid cavity at nose," *Journal of Spacecraft and Rockets*, vol. 52, no. 1, pp. 157–165, 2015.

[15] J. M. Solomon, "The design, calibration, and commissioning of a benchmark hypersonic wind tunnel," Master's thesis, The University of North Carolina at Charlotte, 2021.

[16] J. Redford and X. Li, "Exploration of svd for image compression and time series processing," in *2020 IEEE MIT Undergraduate Research Technology Conference (URTC)*, pp. 1–4, IEEE, 2020.

APPENDIX A: RESIDUALS AND CONVERGENCE

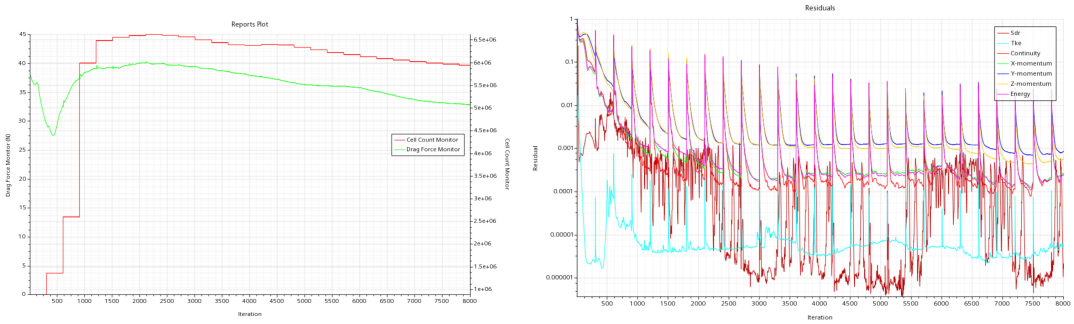

Figure A.1: Residuals and Automated Mesh Refinement Convergence for the No Cavity Ideal Gas Equation of State.

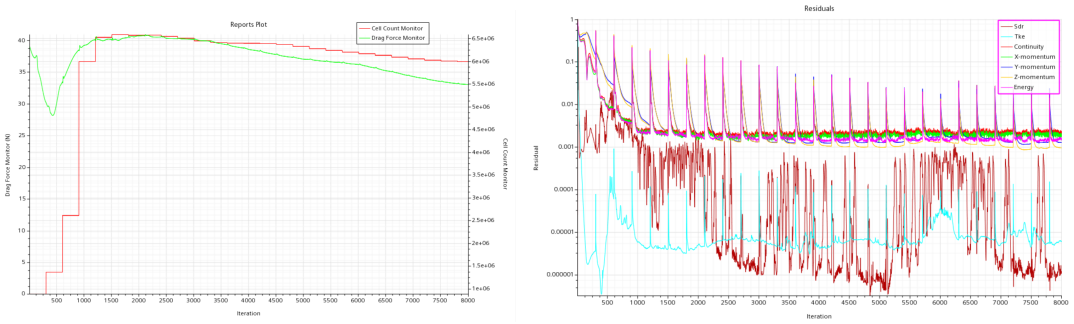

Figure A.2: Residuals and Automated Mesh Refinement Convergence for the No Cavity Real Gas Equation of State.

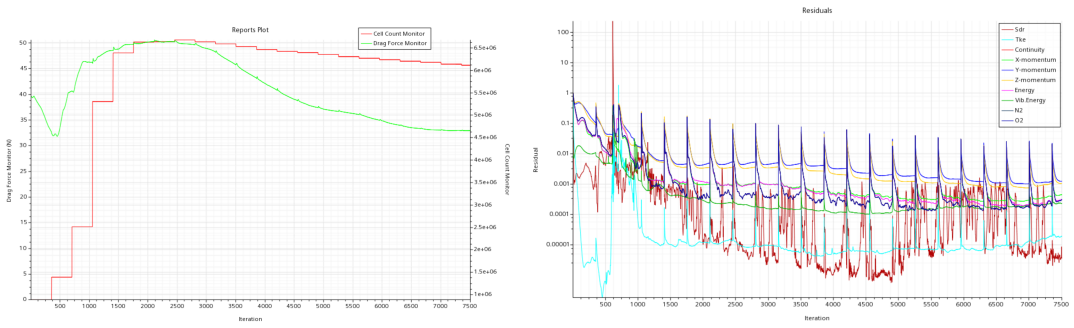

Figure A.3: Residuals and Automated Mesh Refinement Convergence for the No Two Species Thermal Non-equilibrium Gas Equation of State.

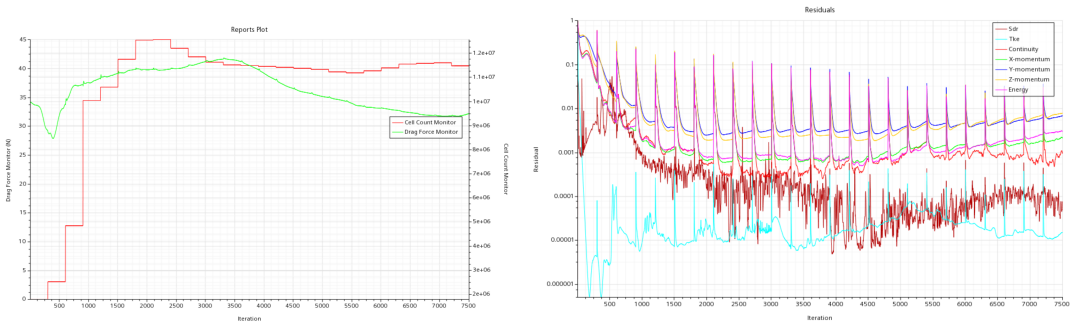

Figure A.4: Residuals and Automated Mesh Refinement Convergence for the Cavity Ideal Gas Equation of State.

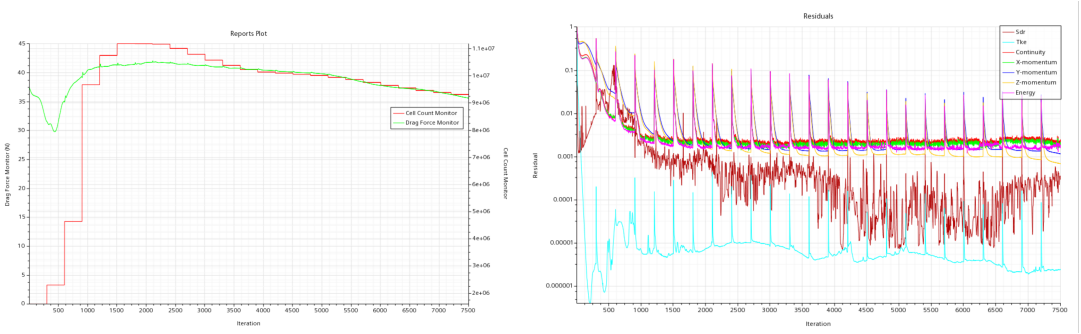

Figure A.5: Residuals and Automated Mesh Refinement Convergence for the Cavity Real Gas Equation of State.

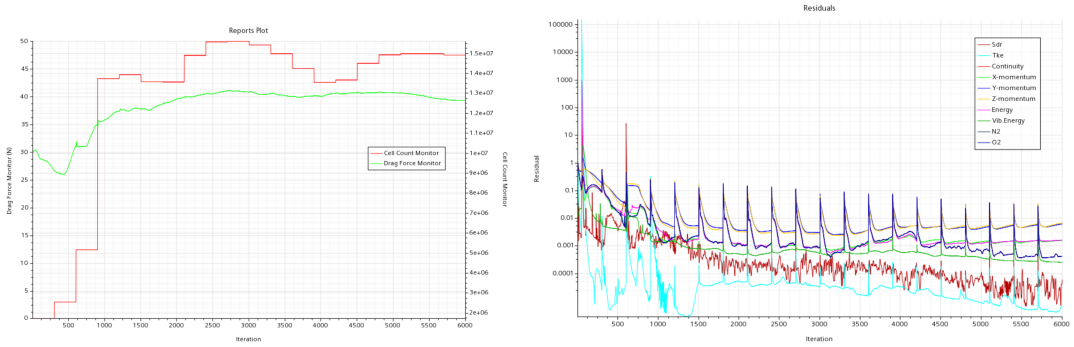

Figure A.6: Residuals and Automated Mesh Refinement Convergence for the Cavity Two Species Thermal Non-equilibrium Gas Equation of State.